

# The Diabatic Rossby Vortex: Growth Rate, Length Scale, and the Wave–Vortex Transition

MATTHIEU KOHL<sup>a</sup> AND PAUL A. O'GORMAN<sup>a</sup>

<sup>a</sup> *Department of Earth, Atmospheric, and Planetary Sciences, Massachusetts Institute of Technology, Cambridge, Massachusetts*

(Manuscript received 24 January 2022, in final form 26 May 2022)

**ABSTRACT:** In idealized simulations of moist baroclinic instability on a sphere, the most unstable mode transitions from a periodic wave to an isolated vortex in sufficiently warm climates. The vortex mode is maintained through latent heating and shows the principal characteristics of a diabatic Rossby vortex (DRV) that has been found in a range of different simulations and observations of the current climate. Currently, there is no analytical theory for DRVs or understanding of the wave–vortex transition that has been found in warmer climates. Here, we introduce a minimal moist two-layer quasigeostrophic model with tilted boundaries capable of producing a DRV mode, and we derive growth rates and length scales for this DRV mode. In the limit of a convectively neutral stratification, the length scale of ascent of the DRV is the same as that of a periodic moist baroclinic wave, but the growth rate of the DRV is 54% faster. We explain the isolated structure of the DRV using a simple potential vorticity (PV) argument, and we create a phase diagram for when the most unstable solution is a periodic wave versus a DRV, with the DRV emerging when the moist static stability and meridional PV gradients are weak. Last, we compare the structure of the DRV mode with DRV storms found in reanalysis and with a DRV storm in a warm-climate simulation.

**SIGNIFICANCE STATEMENT:** Past research has identified a special class of midlatitude storm, dubbed the diabatic Rossby vortex (DRV), which derives its energy from the release of latent heat associated with condensation of water vapor and as such goes beyond the traditional understanding of midlatitude storm formation. DRVs have been implicated in extreme and poorly predicted forms of cyclogenesis along the east coast of the United States and the west coast of Europe with significant damage to property and human life. The purpose of this study is to develop a mathematical theory for the intensification rate and length scale of DRVs to gain a deeper understanding of the dynamics of these storms in current and future climates.

**KEYWORDS:** Eddies; Extratropical cyclones; Instability; Potential vorticity; Diabatic heating; Climate change; Quasigeostrophic models

## 1. Introduction

In small-amplitude calculations of moist baroclinic instability over a wide range of climates in an idealized GCM, O'Gorman et al. (2018) found that the most unstable mode transitions from a quasi-periodic wave to an isolated vortex at a midlatitude surface air temperature of roughly 292 K.<sup>1</sup> The structure of the vortex mode that emerged in warm climates (Fig. 1a) consists of a dipole of interlocking potential vorticity (PV) anomalies above the boundary layer: cyclonic in the lower free troposphere and anticyclonic in the upper troposphere. Warm-air advection to the east of the cyclonic anomaly and to the west of the anticyclonic anomaly leads to ascent and diabatic PV generation from latent heat release in the form of a dipole. We note that, because the mode is found

for warm-climate simulations, the diabatic generation extends higher in the atmosphere than it would in the current climate.

The constellation of PV anomalies and diabatic PV generation is such that the anomalies are amplified and maintained against the background shear flow. The resulting vortex mode bears the principal characteristic of a diabatic Rossby vortex (DRV) that has been found in a range of different simulations and observation. Its emergence as the fastest-growing mode within the moist baroclinic instability calculations of O'Gorman et al. (2018) points to the profound modifying influence that latent heating has on the structure of fast-growing disturbances in a warming climate.

DRVs first emerged as an alternative mode of instability in idealized studies of moist baroclinic instability. The presence of moisture greatly enriches the dynamics of unstable modes because condensation and precipitation are strongly associated with ascending but not descending motion, and hence an additional nonlinearity is introduced into the thermodynamic equation (O'Gorman 2011). Emanuel et al. (1987) represented condensational heating in Eady and two-level semigeostrophic models by assuming saturated moist-adiabatic ascent. This assumption leads to a nonlinear factor  $r(w)$  that is a function of the vertical velocity  $w$  and reduces the potential vorticity [or static stability in quasigeostrophic (QG) models] by a factor  $r < 1$  in updrafts while leaving it unchanged in

<sup>1</sup> The most unstable modes were calculated in O'Gorman et al. (2018) through repeated rescaling of perturbations to small amplitude, assuming upward motion to be saturated, and using a basic state equal to the zonal and time-mean of a fully nonlinear simulation for that climate.

Corresponding author: Matthieu Kohl, mkohl@mit.edu

DOI: 10.1175/JAS-D-22-0022.1

© 2022 American Meteorological Society. For information regarding reuse of this content and general copyright information, consult the AMS Copyright Policy ([www.ametsoc.org/PUBSReuseLicenses](http://www.ametsoc.org/PUBSReuseLicenses)).

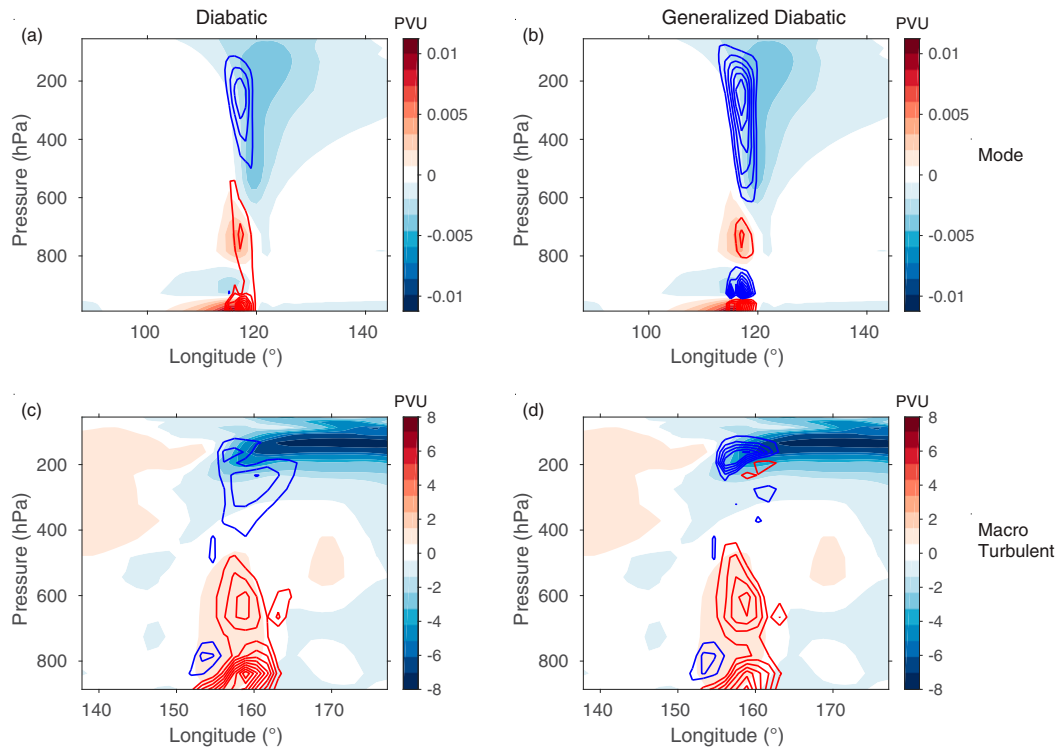


FIG. 1. Potential vorticity (PV) anomalies (shading) and diabatic generation of PV due to latent heating (contours) for (a) the DRV mode at latitude  $44^\circ$  in a calculation of small-amplitude moist baroclinic instability on a sphere in a warm climate (global mean surface temperature 311 K) using an idealized GCM (O’Gorman et al. 2018), and (c) a DRV storm at latitude  $61^\circ$  in the corresponding macro-turbulent (i.e., finite amplitude) simulation at statistical equilibrium in the same GCM. (b),(d) As in (a) and (c) except that they show the generalized diabatic generation of PV calculated according to Eq. (29), which includes both diabatic PV generation and diabatic vertical advection of PV, where the only diabatic process considered is latent heating. The PV is calculated using the hydrostatic approximation to Ertel’s PV, and PV anomalies are with respect to the zonal mean. The contour interval is  $9.2 \times 10^{-5}$  pvu  $\text{h}^{-1}$  in (a) and (b) and  $0.07$  pvu  $\text{h}^{-1}$  in (c) and (d) ( $1 \text{ pvu} = 1.0 \times 10^{-6} \text{ m}^2 \text{ s}^{-1} \text{ K kg}^{-1}$ ). The zero contour is not plotted. Note that since the DRV mode in (a) and (b) was calculated using repeated rescaling of amplitude, the overall amplitude of its fields is arbitrary.

downdrafts ( $r = 1$ ). While this parameterization is a simplification, it captures the essential asymmetry that is introduced through the irreversible fallout of condensate during precipitation, and  $r$  may be calculated from the observed temperature and pressure distributions in the atmosphere. The effect of this condensational heating was to increase the growth rates and decrease the area of ascent of growing modes with respect to dry waves, results that are borne out well by moist baroclinic life cycle studies with shallow water models (Lambaerts et al. 2012) or more comprehensive forecasting models (Booth et al. 2015). When moist instability calculations were done with a more realistic reduction factor  $r(z)$  that varied vertically, the short wavelength cutoff of the Eady model disappeared (Whitaker and Davis 1994; Moore and Montgomery 2004). A new mode of instability emerged at shorter wavelengths that could intensify without the presence of upper-level forcing (Montgomery and Farrell 1991, 1992; Whitaker and Davis 1994; Moore and Montgomery 2004). This mode now grew through the interaction of a surface potential temperature anomaly and an interior PV anomaly,

rather than primarily through an interaction of anomalies of potential temperature at the surface and lid, and the budget of eddy available potential energy was dominated by diabatic rather than baroclinic generation.

Subsequent three-dimensional simulations with a mesoscale model by Moore and Montgomery (2005) showed that this alternative diabatic growth mechanism could generate isolated coherent PV-dipole structures consisting of a phase locked low-level cyclonic anomaly and a midtropospheric anticyclonic anomaly starting from an initial moist baroclinic environment without upper-level forcing. The isolated and diabatic character of such a growing disturbance without upper-level forcing led Moore and Montgomery (2004) to classify it as “diabatic Rossby vortex”—a term that we adopt in this paper. More recently, idealized channel simulations of cyclone development using a weather forecasting model (Tierney et al. 2018) showed signs of breakup into “jagged diabatic” PV structures reminiscent of a DRV at sufficiently warm temperatures, in line with the results of O’Gorman et al. (2018). Going beyond initial-value problems, turbulent simulations on a beta plane

using moist two-layer QG or shallow water equations showed a transition from a smooth large-scale jet flow to a jet flow disrupted by the presence of small-scale vortices that rapidly intensify through moist-dynamical feedbacks in the strongly precipitating regime of the simulation (Lapeyre and Held 2004; Bembenek et al. 2020). In Bembenek et al. (2020) these vortices were explicitly likened to DRVs. We have also found growing DRVs in the fully nonlinear warm-climate simulations of O'Gorman et al. (2018). An example of such a DRV is shown in Fig. 1c, and it exhibits considerable similarity with the DRV mode calculated by repeated rescaling to small amplitude (Fig. 1a), although the positive PV anomaly extends higher into the atmosphere and the negative PV anomaly and diabatic PV generation are more concentrated at the upper tropopause.

DRVs have also been invoked to account for the initial phase prior to explosive growth of certain cyclones in in operational analyses and realistic simulations. Both the European extreme storm "Lothar" in 1999 (Wernli et al. 2002) and the explosive East Coast winter storm in 2005 (Moore et al. 2008) were shown to propagate and intensify moderately through diabatic effects without upper-level forcing before intensifying explosively through upper-level interactions in a secondary growth process. In this paper, we will remain focused on the initial phase of diabatic self-amplification/propagation without considering upper interactions. While the isolated and vortical structure of the East Coast winter storm led Moore et al. (2008) to classify it as a DRV following the terminology of Moore and Montgomery (2004), the rapid propagational character of Lothar, faster than the ambient winds, led Wernli et al. (2002) to classify it as a "diabatic Rossby wave" (DRW) with the positive diabatic PV generation to the east of the low-level cyclonic PV anomaly playing the role of meridional PV advection in a classic dry Rossby wave as discussed in Parker and Thorpe (1995). Both DRV and DRW refer to the same phenomenon, but neither name is fully satisfactory since such storms are isolated like vortices but propagate through PV generation like a wave (Boettcher and Wernli 2013). The upper-level negative PV anomaly is found to be relatively weak in observed storms, and some uncertainty exists in the literature as to when latent heating leads to growth through interaction of the positive low-level PV anomaly with a self-induced negative upper PV anomaly, or rather just leads to propagation of the low-level PV anomaly. The importance of diabatic effects in individual case studies of rapid cyclogenesis, led Boettcher and Wernli (2013) to study DRVs more systematically by compiling a 10-yr (2001–10) climatology of DRV tracks for the North Pacific and North Atlantic Oceans. DRVs occurred at an average rate of 81 systems per year over the North Pacific and 43 system per year over the North Atlantic. In line with the case studies of Lothar and the East Coast winter storm, DRVs in the current climate were found to propagate with moderate intensification before interacting in a second phase with a preexisting upper-level PV anomaly or jet stream.

It is clear from the literature that DRVs constitute an alternative diabatic growth mechanism that relies both on

sufficient baroclinicity and moisture and that produces relatively small-scale modes that can self-amplify exponentially even without the presence of upper-level forcing. Currently, there is no theory for the growth rate and length scale of DRVs or the wave–vortex transition that occurs at higher temperatures in moist baroclinic instability simulations. Analytically tractable models of dry and moist baroclinic instability (Eady 1949; Charney 1947; Phillips 1954; Emanuel et al. 1987; Zurita-Gotor 2005) form much of the basis of our theoretical understanding of cyclones due to their ability to isolate the mechanism of cyclone formation in a conceptually simple model and to relate growth rate and length scale of cyclones to atmospheric parameters in a quantitative way. Given the importance of diabatic effects in cyclogenesis both in the current and future climate, it seems desirable to develop an equivalent conceptually simple model for a DRV.

To this end, we introduce in this paper a minimal moist two-layer QG model with tilted upper and lower boundaries and show that it is capable of producing a DRV mode. Latent heating is represented by an assumption of saturated ascent in updrafts following previous work (Emanuel et al. 1987; Fantini 1995; Zurita-Gotor 2005). We tilt the model boundaries at a slope equal to that of the mean isentropes to make the two-layer model an analog of the interior of the Eady model in which dry-baroclinic instability has been shut off but any moist instability is retained. This allows us to transition to a pure DRV solution within a conceptually simple model. We note that this model is similar in spirit to the unbounded balanced shear flow studied by Snyder and Lindzen (1991) to demonstrate the possibility of growth through diabatically generated interior anomalies in a setup that is dry modally stable. However, Snyder and Lindzen (1991) allowed for negative latent heating in descent regions and so obtained periodic wave solutions rather than an isolated DRV.

We begin in section 2 by formulating the tilted two-layer model and showing that it produces a DRV mode. We then study its PV budget and derive the dispersion relation of the DRV mode analytically, a significant novelty of this paper. Asymptotic solutions for the growth rate and ascent length of the DRV are found in the limit of small  $r$ . We also solve the dispersion relation for the infinite domain numerically by root finding for the whole range of  $r$ . In section 3, we study the emergence of DRV modes in the more general case that includes nonzero meridional PV gradients. We first introduce a simple PV argument to explain the wave–vortex transition observed to occur as latent heating becomes dominant in the moist baroclinic instability simulations of O'Gorman et al. (2018). We then generate a phase diagram for when the most unstable mode in a partially tilted two-layer model is a periodic wave versus a DRV as a function of the PV gradients and  $r$ . In section 4, we compare the warm-climate DRV mode and DRV storm from the idealized GCM simulations of O'Gorman et al. (2018) with two storms in the present climate that have previously been found to have the characteristics of DRVs. Last, in section 5 we summarize our results and discuss their implications.

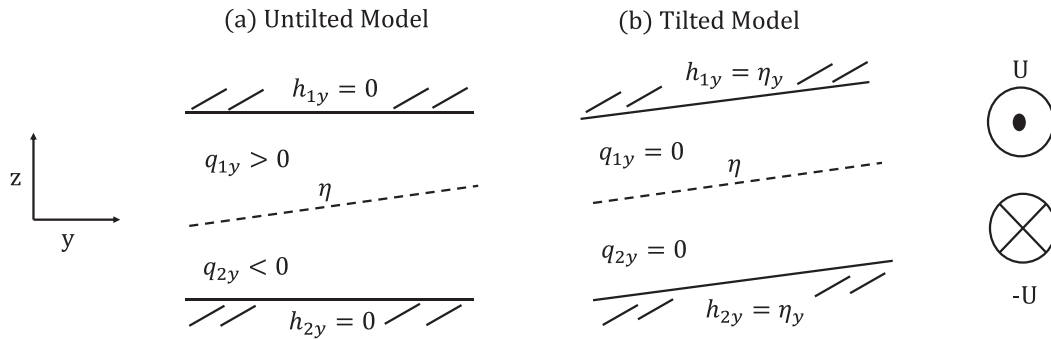


FIG. 2. Schematic of the (a) untilted and (b) tilted two-layer model with basic-state interface height  $\eta$ , boundary slopes  $h_{1y} = h_{2y} = \eta_y$ , and basic-state PV gradients  $q_{1y}$  and  $q_{2y}$ . Also shown is the basic-state zonal mean wind profile (the dot represents flow out of the page, and the cross represents flow into the page), which is the same for the tilted and untilted models.

2. A simple model for a DRV

a. Model formulation

We seek a minimal model that can capture the internal interactions of diabatically generated PV anomalies characteristic of a DRV. We start from the moist quasigeostrophic equations on an  $f$  plane:

$$\partial_t \nabla^2 \psi + J(\psi, \nabla^2 \psi) - fw_z = 0 \quad \text{and} \quad (1)$$

$$\partial_t \psi_z + J(\psi, \psi_z) + \frac{N^2}{f} r(w)w = \frac{N^2}{f} \overline{r(w)w}, \quad (2)$$

where  $\psi$  is the streamfunction,  $w$  is the vertical velocity,  $N^2$  is the constant static stability,  $f$  is the Coriolis parameter,  $J(A, B) = A_x B_y - B_x A_y$  is the Jacobian, and  $(\dots)$  is a horizontal domain average. Equations (1) and (2) are equivalent to Eqs. (16) and (17) of Fantini (1995) except for the addition of the term  $(N^2/f)r(w)w$  on the right-hand side of the thermodynamic equation [Eq. (2)], which acts as a spatially uniform radiative cooling to ensure that the domain-mean temperature remains constant even though there is latent heating. The effects of latent heating on the dynamics are encapsulated in the spirit of simple moist theories (Emanuel et al. 1987; Fantini 1995) by the nonlinear factor

$$r(w) = \begin{cases} r, & w \geq 0 \\ 1, & w < 0 \end{cases}, \quad (3)$$

which reduces the static stability by a factor  $r$  in regions of ascent. Under an assumption of saturated moist-adiabatic ascent,

$$r = \frac{\theta}{\theta^*} \frac{\Gamma_m}{\Gamma_d} \left( \frac{\partial \theta^*}{\partial z} \right) / \left( \frac{\partial \theta}{\partial z} \right)$$

[see Eq. (7) of Fantini 1995], where  $\theta$  and  $\theta^*$  are the potential and saturated equivalent potential temperature, respectively, and  $\Gamma_d$  and  $\Gamma_m$  are the dry-adiabatic and moist-adiabatic lapse rates, respectively. The reduction factor in the ascent region varies strongly in the vertical direction. In cyclones with

strong diabatic heating,  $r$  can go all the way to zero in the interior and tend toward 1 as the tropopause is reached. Averaged in the vertical direction,  $r = 0.1$  is a typical value for the current climate and  $r = 0.01$  for the warm-climate GCM simulations in O’Gorman et al. (2018). In physical terms, the nonlinear factor  $r(w)$  represents the fact that while moist ascending air releases latent heat upon condensation and feels a locally reduced static stability, the descending air is subsaturated (after irreversible fallout of condensate by precipitation) and thus feels the full static stability. Moist thermodynamics thus introduces an additional nonlinearity into the equations that greatly enriches the dynamics.

We simplify the dynamics further by discretizing the equations in the vertical direction into two equal layers of height (Fig. 2), anticipating that the two layers will be sufficient to represent the PV-dipole structure of the DRV. We introduce a barotropic streamfunction  $\phi = (\psi_1 + \psi_2)/2$  and a baroclinic streamfunction  $\tau = (\psi_1 - \psi_2)/2$ , where 1 refers to the upper layer and 2 refers to the lower layer. The layer interface height is  $\eta = -(f/g')(\psi_1 - \psi_2)$ , with  $g' = g(\theta_1 - \theta_2)/\theta_0$  where  $g$  is the gravitational constant,  $\theta_1$  and  $\theta_2$  are potential temperatures in each layer, and  $\theta_0$  is a reference potential temperature.

We assume small perturbations about a basic state  $\tau_0 = -Uy$  corresponding to a flow  $u_1 = -\psi_{1y} = U$  in the upper layer and  $u_2 = -\psi_{2y} = -U$  in the lower layer. The small amplitude of the perturbations allows us to linearize the advection terms, but the thermodynamic equation remains nonlinear because of the latent heating term.

The key novelty of our model is that we tilt the top and bottom boundaries,  $h_1(y)$  and  $h_2(y)$ , respectively, to have slopes in the meridional direction of  $h_{1y} = h_{2y} = \eta_y = -(2f/g')\tau_{0y}$ , so as to match the slope of the basic-state layer interface  $\eta$  (Fig. 2b) in contrast to the standard untilted two-layer model (Fig. 2a). This makes our two-layer model an analog of the interior of the Eady model with zero meridional PV gradients  $q_{1y} = q_{2y} = 0$  in the basic state. The dry modal instability through interlocking Rossby waves is thus shut off, but any instability solely due to the moist processes is retained. The equations for the perturbations about the basic state are derived in

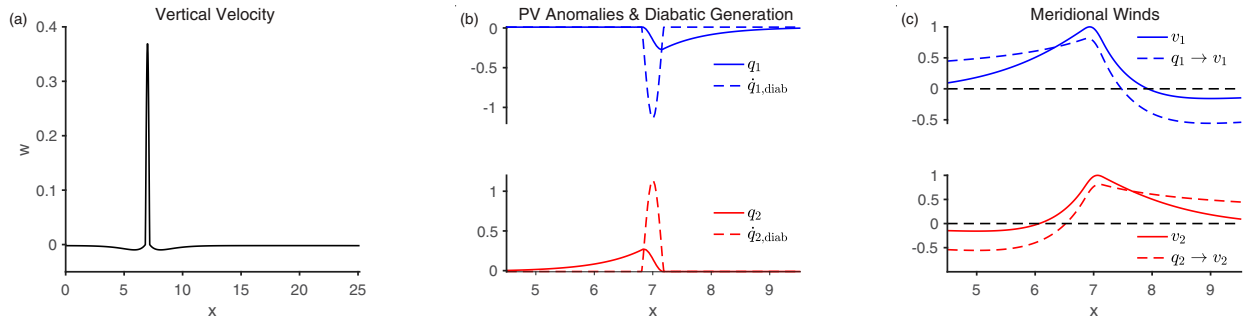


FIG. 3. (a) Vertical velocity, (b) PV anomalies (solid) and diabolic PV generation rate (dashed), and (c) total meridional winds (solid) and meridional winds induced by PV anomalies in the same layer (dashed). All quantities are plotted vs  $x$  for the fastest-growing mode of the tilted-model equations at  $r = 0.01$ , which is a DRV. In (b) and (c), quantities in the upper layer are shown in blue and quantities in the lower layer are shown in red. The domain size is  $L = 8\pi$ , and the grid spacing is  $\Delta x = 0.025$ . All quantities are nondimensional, and the overall magnitude of the DRV is arbitrary. The results in (b) and (c) have been zoomed in around the location of ascending motion to better show the structure of the fields since the DRV occupies only a small fraction of the domain.

appendix A in the limit of small-amplitude perturbations and are given here in nondimensional form:

$$\partial_t \phi_{xx} + \tau_{xxx} - \tau_x = 0, \quad (4)$$

$$\partial_t \tau_{xx} + \phi_{xxx} - \phi_x + w = 0, \quad \text{and} \quad (5)$$

$$\partial_t \tau - \phi_x + r(w)w = \overline{r(w)w}, \quad (6)$$

where  $\tau$ ,  $\phi$ , and  $w$  are now perturbations about the basic state.<sup>2</sup> We note that a dry two-layer model with sloping upper and lower boundaries was already introduced by Bretherton (1966) to allow independent variation of PV gradients and vertical shear in an investigation of the short-wavelength cut-off of baroclinic instability. Evidently, the reason for introducing the tilted boundaries here is different, as we are interested in eliminating the basic-state PV gradients all together.

### b. Numerical simulation

We first solve the tilted-model equations numerically to isolate and study the fastest-growing mode for a given static-stability reduction factor  $0 \leq r \leq 1$ . To this end, we discretize the equations using second-order central finite differences in a periodic domain in  $x$ .

We integrate the barotropic and baroclinic vorticity equations [Eqs. (4) and (5)] forward in time for the variables  $\Phi = \phi_{xx}$  and  $\mathbf{T} = \tau_{xx}$ . Time stepping is performed with MATLAB'S "ode45" function, which is based on an explicit Runge–Kutta (4, 5) formula with an adaptive time step.

The system of equations is closed by calculating the vertical velocity  $w$  at each time step from the nonlinear omega equation,

$$[r(w)w]_{xx} - w = 2\phi_{xxx} - \phi_x, \quad (7)$$

which is formed by eliminating the time derivatives between Eqs. (5) and (6). By using the omega equation, time stepping of Eq. (6) is not needed. The nonlinearity in the omega equation arises from  $r(w)$  and requires an iterative approach to finding the solution. We solve it iteratively at each time step as  $[r(w^n)w^{n+1}]_{xx} - w^{n+1} = \text{rhs}$ , where  $n$  is the iteration step. We start the iteration from a random guess for  $w$  to define the initial  $r(w)$ , and we iterate until the root-mean-square (rms) of  $(w^{n+1} - w^n)$  is smaller than  $10^{-12}$ .

We start the time stepping from random initial conditions for  $\Phi$  and  $\mathbf{T}$ . At each time step, we invert  $\Phi = \phi_{xx}$  and  $\mathbf{T} = \tau_{xx}$  to obtain  $\phi$  and  $\tau$  by imposing that  $\phi$  and  $\tau$  have zero mean. We then solve for  $w$  using the iterative approach to the omega equation described above, and we then update  $\Phi$  and  $\mathbf{T}$  using Eqs. (4) and (5). We rescale the amplitudes of the vectors  $\Phi$  and  $\mathbf{T}$  by a factor of 100 each time rms  $(\mathbf{x}) > 10$ , where  $\mathbf{x} = (\mathbf{T}, \Phi)$ , to avoid large numbers that could cause problems with the numerical representation. We integrate until the nondimensional time is  $t = 200$  when we find that the solution has converged to a normal mode.

The vertical velocity (at time  $t = 200$ ) for  $r = 0.01$  is shown in Fig. 3a where we have used a grid spacing of  $\Delta x = 0.025$  and a domain size of  $8\pi$ . Remarkably, the solution evolves into a DRV with a single spatially localized peak in vertical velocity just like in the warm limit of the idealized GCM calculations of O'Gorman et al. (2018, their Figs. 1f and 2f). The isolated solution is in stark contrast to the spatially periodic structure of moist baroclinic waves. The solution is exponentially growing and fixed in space because the basic-state zonal wind is equal and opposite in each layer, but the DRV would propagate zonally with a more realistic vertical wind profile. We have repeated the calculations using a linear drag on the relative vorticity in the lower layer with a damping time scale of either 10 days (weak drag) or 2.5 days (strong drag).

<sup>2</sup> Equations (4) and (5) are identical to the two-layer moist QG equations (Zurita-Gotor 2005) except for the addition of the terms  $-\tau_x$  and  $-\phi_x$  in Eq. (4) and Eq. (5), respectively, which arise because of the tilted boundaries, and except for the presence of the mean radiative cooling term  $r(w)w$  in Eq. (6). Zurita-Gotor (2005) studied the stability of moist waves by combining the equations into a single equation for  $w$  in which case any mean radiative cooling term drops out for an untilted model. We will see shortly, however, that the mean radiative cooling does not drop out when forming the  $w$  equation for the tilted model.

Isolated DRV solutions persist even with drag included, with similar length scale but reduced growth rate relative to the default case with no drag (not shown).

We next analyze the PV dynamics of the DRV mode. The PV budget in the lower layer was obtained by rewriting the  $r(w)w$  term as  $r(w)w = w - [1 - r(w)]w$  in the thermodynamic equation [Eq. (6)], eliminating the  $w$  term using the baroclinic vorticity equation [Eq. (5)], and adding the barotropic vorticity equation [Eq. (4)] to give

$$\frac{\partial q_2}{\partial t} = \sigma q_2 = q_{2x} + [1 - r(w)]w + \overline{r(w)w}, \quad (8)$$

where  $q_2 = \phi_{xx} - \tau_{xx} + \tau$  is the lower-layer PV,  $\sigma$  is the growth rate,  $q_{2x}$  is zonal advection, and  $\overline{q_{2,\text{diab}}} = [1 - r(w)]w + \overline{r(w)w}$  is the diabatic generation rate. A similar equation may be derived for the upper-layer PV anomaly  $q_1 = \phi_{xx} + \tau_{xx} - \tau$ , which has diabatic generation given by  $\overline{q_{1,\text{diab}}} = -[1 - r(w)]w - \overline{r(w)w}$ . The DRV mode is made up of a positive PV anomaly in the lower layer and a negative PV anomaly in the upper layer that are both growing through diabatic PV generation (Fig. 3b). Note that meridional PV advection does not appear in the PV budget because the meridional PV gradients are zero by construction in the tilted model, but for completeness, we also show the meridional winds (Fig. 3c). Exploration of the parameter space of  $r$  shows that the basic PV structure remains similar for all values of  $0 \leq r < 1$ , although the growth rate and horizontal length scale of the ascent region do change when  $r$  is varied. At  $r = 1$  the system is dry and stable because there are no contributions from latent heating, and by construction there are no meridional PV gradients to otherwise support baroclinic instability.

We calculate the growth rate of the mode by assuming exponential growth of the rms of  $\mathbf{x} = [\Phi, \mathbf{T}]$  over each time step  $\Delta t$  to give  $\sigma = \log\{\text{rms}[\mathbf{x}(t)]/\text{rms}[\mathbf{x}(t - \Delta t)]\}/\Delta t$ . Note that the time stepping is adaptive and the step size  $\Delta t$  can vary. We then average  $\sigma$  over the end period of the calculation ( $t = 195\text{--}200$ ).

From Fig. 4 we see that within the narrow region of ascent the growth of the positive PV anomaly is due to diabatic PV generation through latent heating that is partially offset by zonal advection. In the region of descending motion to the west, the PV generation due to latent heating is zero and the growth of the PV anomaly is due to zonal advection over a more extended spatial scale. The PV tendency from radiative cooling is spatially constant with a value of  $\overline{r(w)w} = -0.011$ . In the region of descent to the east, all the terms in the lower-layer PV budget are zero except for the time tendency and the small term due to radiative cooling. The PV budget in the upper layer is the same as in the lower layer except that the signs of the terms are flipped and they are mirrored about the axis of maximum ascent.

Now that we have isolated the DRV solution within a simplified model, it is possible to develop analytical solutions for its characteristics.

### c. Analytic theory

We now derive the growth rate and horizontal length scale of the DRV mode. In the modal regime, the DRV satisfies the equations

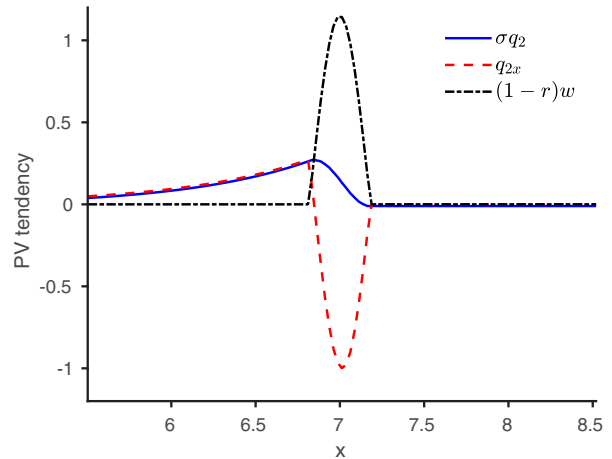


FIG. 4. Terms in the lower-layer PV budget vs  $x$  for the fastest-growing mode of the tilted-model equations at  $r = 0.01$ , which is a DRV. The domain size is  $L = 8\pi$ , and the grid spacing is  $\Delta x = 0.025$ . The terms in the PV budget that are shown are the total tendency (blue) and the contributions from zonal advection (red dashed) and latent heating (black dashed-dotted). The PV tendency from radiative cooling is a small constant with a value of  $\overline{r(w)w} = -0.011$  (not shown). All quantities are nondimensional, and the overall magnitude of the DRV is arbitrary. The PV budget has been zoomed in around the location of ascending motion since the DRV occupies only a small fraction of the domain.

$$\sigma \phi_{xx} + \tau_{xxx} - \tau_x = 0, \quad (9)$$

$$\sigma \tau_{xx} + \phi_{xxx} - \phi_x + w = 0, \quad \text{and} \quad (10)$$

$$\sigma \tau - \phi_x + r(w)w = \overline{r(w)w}. \quad (11)$$

We eliminate the streamfunctions and combine the equations into a single equation for  $w$ :

$$(rw)_{xxxx} - (2 + \sigma^2)(rw)_{xx} + w_{xx} + (r + \sigma^2 - 1)w = \overline{rw}, \quad (12)$$

as shown in appendix B. This equation is similar to the equation for  $w$  derived for moist baroclinic modes in an untilted two-layer model [cf. with Eq. (12) in Zurita-Gotor 2005] except for the two extra terms  $-2(rw)_{xx}$  and  $(r - 1)w$  on the left-hand side of the equation and the radiative cooling term  $\overline{r(w)w}$  on the right-hand side, which is constant in space but varies in time. As we will see shortly, the extra terms on the left-hand side are responsible for producing exponentially decaying rather than periodic solutions in the descent area that are characteristic of an isolated DRV.

We look for symmetric solutions about the peak in  $w$  since that is what was obtained in the numerical solutions and since the equation for  $w$  is symmetric under  $x \rightarrow -x$ . We put the peak in  $w$  at  $x = 0$ , and by symmetry we need only consider the half of the domain  $x \geq 0$ , where  $w$  is ascending between  $0 \leq x \leq b$  and descending for  $x > b$  (see Fig. 5). Here  $b$  is the location of the boundary between ascent and descent that must be found as part of the solution.

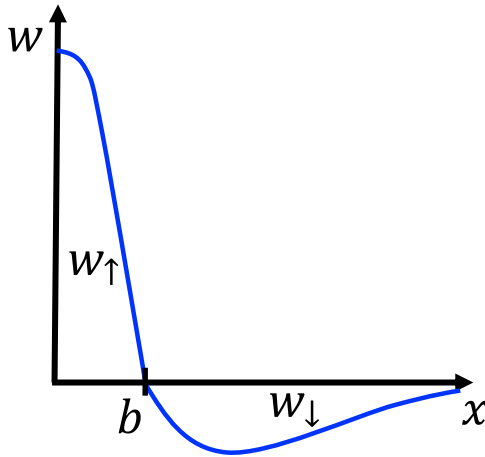


FIG. 5. Schematic of the solution of the  $w$  equation [see Eq. (12)] for the DRV mode. For  $0 \leq x \leq b$  we have ascending motion  $w = w_\uparrow > 0$  and  $r < 1$ , and for  $x > b$  we have descending motion  $w = w_\downarrow < 0$  and  $r = 1$ . Here,  $x = b$  is the location of the boundary between ascent and descent that must be found as part of the solution.

Equation (12) is readily solved separately in the descending and ascending region. In the descending region, the solution is given by

$$w_\downarrow = \frac{a}{\sigma^2} + d_1 e^{-(x-b)} + d_2 e^{-\sigma(x-b)}, \quad (13)$$

where  $a = \overline{r(w)}w$  and we have discarded exponential solutions that become unbounded as  $x \rightarrow \infty$  assuming growing solutions  $\sigma \geq 0$ . In the ascending region, the solution is symmetric about  $x = 0$  and is given by

$$w_\uparrow = \frac{a}{r + \sigma^2 - 1} + c_1 \cos(k_1 x) + c_2 \cos(k_2 x), \quad (14)$$

with wavenumbers

$$k_1 = \frac{1}{\sqrt{2r}} \times \sqrt{1 - r(2 + \sigma^2) + \sqrt{[1 - r(2 + \sigma^2)]^2 - 4r(\sigma^2 + r - 1)}} \quad (15)$$

and

$$k_2 = \frac{1}{\sqrt{2r}} \times \sqrt{1 - r(2 + \sigma^2) - \sqrt{[1 - r(2 + \sigma^2)]^2 - 4r(\sigma^2 + r - 1)}}, \quad (16)$$

which are functions of  $r$  and  $\sigma$ .

We define the domain half-size to be  $L$  and then take the limit of an infinite domain  $L \rightarrow \infty$ . Mass conservation expressed as  $\int_0^L w \, dx = 0$  allows us to rewrite

$$a = \frac{1}{L} \int_0^L r w \, dx = \frac{1}{L} \int_0^L (r - 1) w \, dx = \frac{1}{L} \int_0^b (r - 1) w_\uparrow \, dx,$$

which implies that  $a \rightarrow 0$  as  $L \rightarrow \infty$  if we want solutions for which  $b$  and  $w_\uparrow$  remain bounded. We need additional constraints to determine the constants  $c_1, c_2, d_1, d_2, \sigma$ , and  $b$ . We impose that  $w_\uparrow = w_\downarrow = 0$  at  $x = b$ , continuity of  $(rw)_x$  and  $(rw)_{xx}$  at  $x = b$  and mass conservation. The continuity conditions follow from the continuity of  $\phi, \tau$  and the existence of the derivatives in the governing Eqs. (9)–(11). The constraint that  $w_\downarrow = 0$  at  $x = b$  gives

$$d_1 = -d_2 - \frac{a}{\sigma^2}. \quad (17)$$

Furthermore, the amplitude of the  $w$  solution is arbitrary, which allows us to fix one of the amplitudes without loss of generality. We choose  $d_2 = 1$  when  $\sigma > 1$  and  $d_2 = -1$  when  $\sigma < 1$  to ensure that  $w_\downarrow < 0$ . In the limit of  $L \rightarrow \infty$  and  $a \rightarrow 0$ , the resulting equations are

$$c_1 \cos(k_1 b) + c_2 \cos(k_2 b) = 0, \quad (18)$$

$$c_1 k_1 \sin(k_1 b) + c_2 k_2 \sin(k_2 b) = d_2 \frac{\sigma - 1}{r}, \quad (19)$$

$$c_1 k_1^2 \cos(k_1 b) + c_2 k_2^2 \cos(k_2 b) = d_2 \frac{1 - \sigma^2}{r}, \quad \text{and} \quad (20)$$

$$\frac{c_1}{k_1} \sin(k_1 b) + \frac{c_2}{k_2} \sin(k_2 b) = d_2 \frac{\sigma(\sigma - 1)}{\sigma^2 + r - 1}, \quad (21)$$

expressing  $w_\uparrow = 0$  at  $x = b$ , continuity of  $[r(w)w]_x$ , continuity of  $[r(w)w]_{xx}$ , and mass conservation, respectively. The limit of  $L \rightarrow \infty$  and  $a \rightarrow 0$  in the mass conservation equation must be taken carefully—a subtle point that is discussed in appendix C.

Eliminating the constants  $c_1$  and  $c_2$ , which also gets rid of the arbitrary constant  $d_2$  (see appendix D), we obtain two equations:

$$\tan(k_1 b) = \frac{rk_1 k_2}{\sigma + 1} \left( -\frac{1}{rk_2} + \frac{\sigma k_2}{\sigma^2 + r - 1} \right) \quad \text{and} \quad (22)$$

$$\tan(k_2 b) = \frac{rk_1 k_2}{\sigma + 1} \left( -\frac{1}{rk_1} + \frac{\sigma k_1}{\sigma^2 + r - 1} \right), \quad (23)$$

which along with the definitions of  $k_1$  and  $k_2$  [Eqs. (15) and (16)] yield the dispersion relationship for the growth rate  $\sigma$  and half-ascent length  $b$  as a function of the static-stability reduction factor  $r$ , a key novel result of this paper.

In general, this dispersion relationship needs to be solved numerically, but in the limit of a convectively neutral stratification  $r \rightarrow 0$  it is possible to show analytically that at leading order the growth rate is

TABLE 1. Comparison of the nondimensional and dimensional growth rate  $\sigma$  and half-ascent length in two-layer models for the most unstable dry wave (Phillips 1954), moist wave (Emanuel et al. 1987), and DRV. The half-ascent length is given by one-quarter of the wavelength for the dry wave, and by one-half of the length of the region of ascent for the DRV and moist wave (for the DRV it is  $b$ ). Dimensional values for the growth rate [ $\sigma(U/L_D)$ ] and ascent length ( $bL_D$ ) are calculated using typical scales  $L_D = NH/(\sqrt{2}f) = 1000 \text{ km}/\sqrt{2}$  and  $U = 10 \text{ m s}^{-1}$ . The factor of  $\sqrt{2}$  in  $L_D$  follows from our choice of nondimensionalization. Growth rates for the moist wave and DRV are presented in the limit of a convectively neutral stratification ( $r \rightarrow 0$ ). Half-ascent lengths for the moist wave and DRV are presented as the small- $r$  asymptotic expressions for the nondimensional results and are evaluated at  $r = 0.01$  (representative of a warm climate) for the dimensional results, since the ascent length would be zero for  $r \rightarrow 0$ .

	Growth rate $r \rightarrow 0$	Growth rate ( $\text{day}^{-1}$ ) $r \rightarrow 0$	Half-ascent length $r \ll 1$	Half-ascent length (km) $r = 0.01$
Dry wave	$\sqrt{2} - 1 = 0.41$	0.50	$\frac{\pi}{2\sqrt{\sqrt{2} - 1}}$	1726
Moist wave	1.05	1.28	$\frac{\pi}{2}\sqrt{r}$	111
DRV	$0.5(1 + \sqrt{5}) = 1.62$	1.98	$\frac{\pi}{2}\sqrt{r}$	111

$$\sigma = \frac{1 + \sqrt{5}}{2} = 1.62, \quad (24)$$

and the half-ascent length is

$$b = \frac{\pi}{2}\sqrt{r}, \quad (25)$$

(see appendix E).<sup>3</sup> For comparison, the growth rate  $\sigma$  and half-ascent length (equal to  $b$  for the DRV) for the fastest-growing modes in an untilted dry two-layer model (Phillips 1954) and moist two-layer model (Emanuel et al. 1987) are given in Table 1. Note that the half-ascent length is just one-quarter of the wavelength for the dry mode and that the results in Emanuel et al. (1987) need to be rescaled by a factor  $\sqrt{2}$  to agree with our nondimensionalization. The DRV grows about 4 times as fast as the dry wave and 1.5 times as fast as the moist wave in the small  $r$  limit, consistent with the fact that the DRV emerges as the fastest-growing solution in the warm-climate simulations of moist baroclinic instability in O’Gorman et al. (2018). The ascent length of the DRV and moist wave are the same in the small  $r$  limit and are smaller than that of a dry wave by about a factor of 15 for  $r = 0.01$ .

To obtain  $\sigma$  and  $b$  for the full range of  $r$ , we solve the dispersion equations numerically. Equations (22) and (23) are solved using MATLAB’S `fsolve`. We start by solving at  $r = 10^{-3}$  with initial guess  $\sigma = 1.53$  and  $b = 0.06$  for the first two values of  $r$ , and we use linear extrapolation for the initial guesses at each subsequent value of  $r$ . The results are compared with the time-marching solutions of Eqs. (4), (5), and (7) for a finite domain with periodic boundary conditions in Fig. 6, where we use a larger domain  $L = 32\pi$  with  $\Delta x = 0.084$  for all values of  $r$  to resolve the large and weakly growing solutions as  $r \rightarrow 1$ . Note that the time-marching solution at  $r = 1$  is not growing and is not shown in Fig. 6. The growth rates from the time-marching and dispersion-relation approaches are in good agreement for values below a critical value of  $r = 0.38$ , whereas the

ascent lengths are in good agreement only for values of  $r$  less than roughly 0.2. A sample vertical-velocity profile at  $r = 0.01$  (Fig. 7) confirms that the  $w$  profiles from the time marching and dispersion relations are in very good agreement at small  $r$ . As the critical value of  $r = 0.38$  is approached, the root-finding solution for  $b$  tends to large numbers. For values of  $r > 0.38$ , we only find solutions to the dispersion relation for which the half-ascent length  $b < 0$ . These solutions are unphysical and can be discarded.

In mathematical terms, the breakdown of the solution on an infinite domain at  $r = 0.38$  can be traced to the point at which  $\sigma^2 + r - 1 = 0$  and the right-hand sides of Eqs. (22) and (23) diverge to infinity. Empirically we find that as this point is approached both  $k_1$  and  $k_2$  also go to zero, such that  $b \rightarrow \infty$  is needed to balance a diverging right-hand side. Setting  $k_1 = k_2 = 0$  we obtain  $r = (3 - \sqrt{5})/2 = 0.38$  and  $\sigma = \sqrt{(\sqrt{5} - 1)/2} = 0.79$  for the breakdown point in good agreement with the numerical results. Beyond this point  $\sigma^2 + r - 1 < 0$ , which implies from Eqs. (15) and (16) that  $k_2$  becomes imaginary while  $k_1$  remains real. Hence, “tan” in Eq. (23) switches to “tanh” while the right-hand side of Eq. (23) becomes negative. To satisfy the equation for growing modes, this requires  $b < 0$ , which is unphysical.

Thus, while DRV solutions continue to exist for  $r > 0.38$  on a finite domain with periodic boundary conditions, isolated DRV solutions on an infinite domain cease to exist.

### 3. The role of meridional PV gradients and the wave–vortex transition

So far we have discussed the emergence of DRVs in a moist two-layer model with zero meridional PV gradients in which PV is generated purely from diabatic effects. While such a setup is a useful idealization for a DRV mode, we are interested in studying how the occurrence of DRVs generalizes to a more realistic situation with PV gradients. We start by considering a qualitative PV argument for how the dynamics changes as diabatic effects become dominant over meridional PV advection, and we then extend our tilted two-layer model to include meridional PV gradients.

<sup>3</sup> The dimensional growth rate for  $r \rightarrow 0$  is  $1.62\sqrt{2}Uf/(NH)$ , and the dimensional half-ascent length is  $\pi\sqrt{r}/(2\sqrt{2}) \times NH/f$ , where  $H$  is the depth of one layer and the vertical shear is  $2U/H$ .

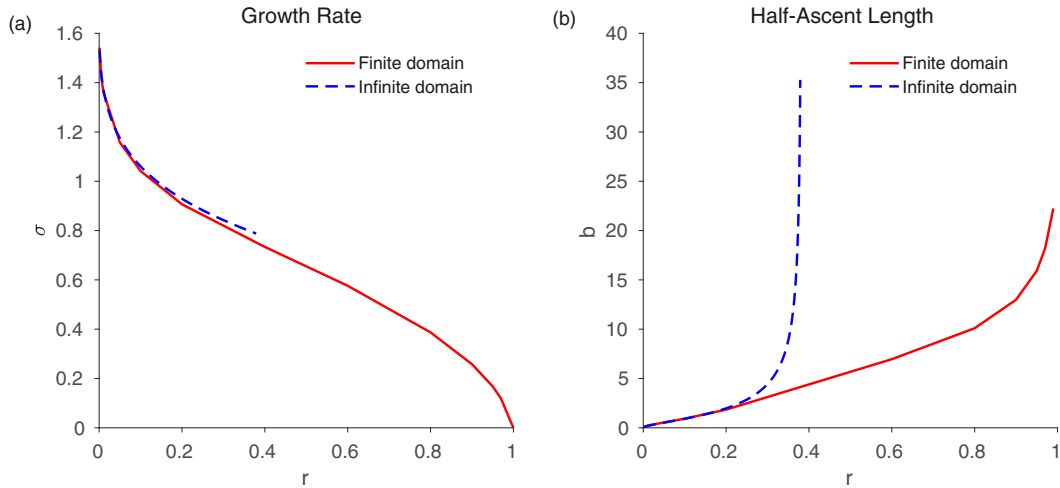


FIG. 6. (a) Growth rate  $\sigma$  and (b) half-ascent length  $b$  from the time-marching solutions of the tilted-model equations [Eqs. (4), (5), and (7)] in a finite periodic domain  $L = 32\pi$  with  $\Delta x = 0.084$  (solid red) and from the root-finding of the dispersion Eqs. (22) and (23) for an infinite domain (dashed blue).

*a. PV dynamical perspective on the wave–vortex transition*

The transition from a periodic wave to an isolated vortex mode in simulations of moist baroclinic instability in which diabatic effects become dominant can be interpreted elegantly within the PV framework of a moist two-layer model (see Fig. 8). Focusing on the lower layer (the upper layer is analogous), we start from the initial condition of a PV wave train consisting of positive and negative anomalies (Fig. 8a).

In a regime in which PV gradients are dominant, meridional advection of the negative background PV gradient in the lower layer would generate a positive PV tendency to the east of a positive PV anomaly, and a negative PV tendency to its west. These advective PV tendencies give rise to a eastward

propagating Rossby wave that can phase lock and grow by interacting with a counterpropagating Rossby wave in the upper layer.

If instead we are in a regime in which the diabatic generation of PV is dominant, ascent to the east of a positive PV anomaly causes latent heat release that generates a positive PV tendency in the lower layer, whereas descent to its west does not generate latent heating and thus there is no negative PV tendency in the lower layer. Thus, only positive PV anomalies survive in the lower layer (with repeated amplitude

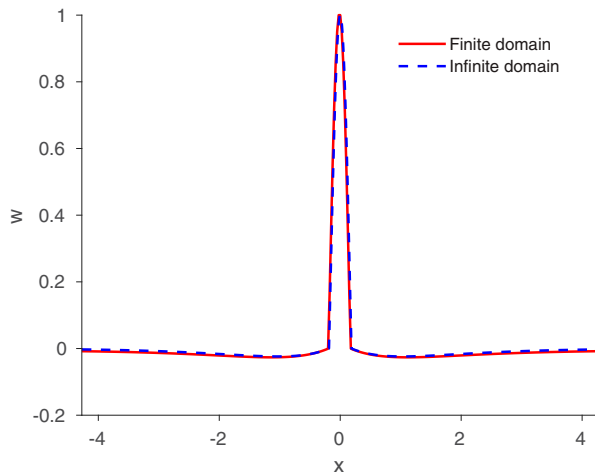


FIG. 7. Comparison of the vertical velocity vs  $x$  for  $r = 0.01$  from the time-marching solution [Eqs. (4), (5), and (7)] in a finite periodic domain (solid red) and from the root-finding of the dispersion relation [Eqs. (22) and (23)] for an infinite domain (dashed blue).

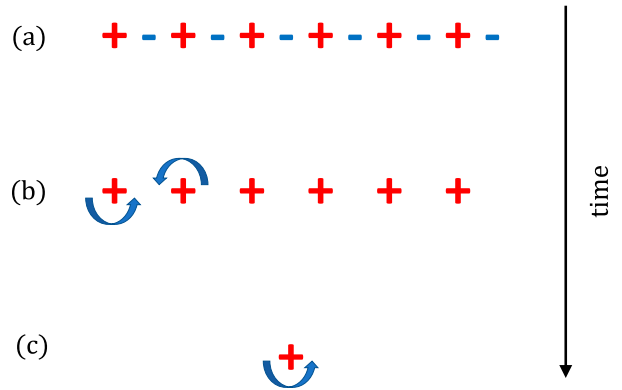


FIG. 8. A PV perspective on the transition from a periodic wave to an isolated vortex in simulations of moist baroclinic instability. Cyclonic PV anomalies are shown as red plus signs, and anticyclonic PV anomalies are shown as blue minus signs. Blue arrows illustrate the direction of horizontal winds induced by the anomalies. Starting from an initial condition consisting of (a) a wave train of PV anomalies in the lower layer, (b) only positive anomalies survive because of the asymmetry in diabatic generation. However, a series of positive anomalies have weaker meridional flow between them that leads to weaker diabatic PV generation as compared with an isolated anomaly, and thus (c) one anomaly is a faster-growing mode of the system.

rescaling to calculate the growing mode) due to the asymmetry in diabatic PV generation (Fig. 8b).

However, a series of positive PV anomalies have weaker meridional flow between them (because of cancellation of the induced flow from neighboring PV anomalies; Fig. 8b) as compared with the meridional flow surrounding an isolated single PV anomaly. Thus, one PV anomaly is a faster-growing mode of the system when diabatic PV generation is dominant over meridional PV advection (Fig. 8c).

#### b. Including PV gradients in the two-layer tilted model

A range of PV gradients can be easily included in our two-layer model by tilting the top and bottom boundaries at variable slopes  $h_{1y} = \alpha_1$  and  $h_{2y} = \alpha_2$ . We retain the basic state  $\tau_0 = -y$  (nondimensionalized) and  $\phi_0 = 0$  corresponding to a shear flow in thermal wind balance. The perturbation equations around this basic state are derived in appendix A and take the form

$$\partial_t \phi_{xx} + \tau_{xxx} - \frac{1}{2}(\alpha_1 - \alpha_2)\phi_x - \frac{1}{2}(\alpha_1 + \alpha_2)\tau_x = 0, \quad (26)$$

$$\partial_t \tau_{xx} + \phi_{xxx} - \frac{1}{2}(\alpha_1 - \alpha_2)\tau_x - \frac{1}{2}(\alpha_1 + \alpha_2)\phi_x + w = 0, \quad \text{and} \quad (27)$$

$$\partial_t \tau - \phi_x + r(w)w = \overline{r(w)w}, \quad (28)$$

with PV gradients  $q_{1y} = 1 - \alpha_1$  and  $q_{2y} = -1 + \alpha_2$ .

We solve the equations numerically for given values of  $r$ ,  $\alpha_1$ , and  $\alpha_2$  using time marching as in section 2b. We use a domain size of  $L = 8\pi$ , but to calculate solutions for a large parameter space we use a larger grid spacing ( $\Delta x = 0.13$ ) than before. We classify the most unstable solution as either an isolated DRV (single local maximum in  $w$ ) or a periodic wave (multiple local maxima in  $w$ ) or stable. Local maxima in  $w$  for which  $w < 0$  are not counted. Cases that are stable or very weakly growing ( $\sigma < 0.09$ ) are counted as stable. The results of this classification are shown in Fig. 9 along with the growth rate  $\sigma$  in Figs. 9a–c and half-ascent length  $b$  in Figs. 9d–f.

We begin by focusing on the equally tilted case  $\alpha_1 = \alpha_2 = \alpha$  for which  $q_{1y} = -q_{2y} = 1 - \alpha$ . We let  $0 \leq \alpha \leq 2$ , which includes the classic untilted regime with  $q_{1y} = 1$  and  $q_{2y} = -1$  at  $\alpha = 0$ , the no-PV-gradient regime  $q_{1y} = q_{2y} = 0$  from the previous section at  $\alpha = 1$ , and a reversed-PV-gradient regime  $q_{1y} = -1$  and  $q_{2y} = 1$  at  $\alpha = 2$ . For  $\alpha < 1$ , a DRV emerges as the fastest-growing solution when the magnitudes of the upper and lower PV gradients are weaker than a threshold  $q_{\text{ycrit}}$  of roughly 0.7 such that  $q_{1y} = -q_{2y} < q_{\text{ycrit}}$  as shown in Fig. 9a.<sup>4</sup>

<sup>4</sup> Note that the solutions classified as DRVs at  $r = 1$  could instead be considered to be waves. From the dry dispersion relation, the wavelength of these most unstable dry modes becomes infinite (not shown), and thus one maximum in  $w$  is found numerically in the domain no matter how large of a domain is chosen. Note also that the pure DRV solution with  $q_{1y} = q_{2y} = 0$  at  $r = 0.9$  is shown to be stable but would grow weakly on a larger domain.

When instead the magnitudes of the upper and lower PV gradients are greater than the critical threshold ( $q_{1y} = -q_{2y} > q_{\text{ycrit}}$ ), the periodic wave emerges as the fastest-growing solution for all values of  $r$ . For the cases with  $\alpha > 1$  in which the PV gradients are reversed from their usual directions, a DRV is the fastest-growing solution, but it is necessary for  $r$  to be sufficiently low for the solution to be unstable, consistent with the dry solutions ( $r = 1$ ) being Fjørtoft stable (Fjørtoft 1950; Pedlosky 1964) because of the mismatch between the directions of the shear and PV gradients. Evidently, this mismatch is also sufficient to inhibit the growth of the moist modes unless  $r$  is sufficiently low such that the dynamics is dominated by latent heating. Overall, these results confirm that the emergence of isolated DRV modes in the tilted model is not an artifact of having exactly zero PV gradients—although this is a useful limit to consider for theory—but rather generalizes to more realistic configurations that do include PV gradients. Again, we have repeated the calculations using a linear drag acting on the relative vorticity in the lower layer with a damping time scale of either 10 days (weak drag) or 2.5 days (strong drag). The wave–vortex transition persists, with the precise boundary largely unaffected by drag. Length scales are similar, but the growth rates are reduced (not shown).

Surprisingly, Fig. 9a suggests that the transition from wave to DRV regime in the two-layer model with equal and opposite PV gradients is independent of  $r$  (the boundary at  $q_{\text{ycrit}}$  is entirely horizontal) but does rely on weakening or reversing the PV gradients relative to the classic untilted two-layer model. We investigate this result further by repeating the calculations with PV gradients that are not equal and opposite, but rather allowed to vary independently from each other, for two example values of  $r$  (Figs. 9b,c). We observe that lowering of  $r$ , as expected in a warmer climate whose stratification is closer to moist adiabatic, does make a difference since it produces DRVs as the fastest-growing solution for a larger range of PV gradients, particularly away from the diagonal line where the PV gradients are exactly equal and opposite. We also recall from the analytical solutions the existence of an upper bound on  $r$  for DRVs to occur in an infinite domain when the PV gradients are zero (Fig. 6). Overall, we find that both weak PV gradients and weak moist static stability (small  $r$ ) can favor DRVs.

#### 4. Comparison with storms at finite amplitude

Our two-layer theory for DRV modes and the warm-climate DRV mode in the idealized GCM calculation of O’Gorman et al. (2018) are both based on an assumption of small-amplitude disturbances. In this section, we analyze DRV storms in reanalysis and a warm-climate simulation of the idealized GCM to see how finite amplitude affects storm structure. We are particularly interested in the question of whether finite-amplitude effects can weaken the upper-level anticyclonic PV anomaly and possibly lead to DRVs that propagate but do not grow strongly because of the lower PV anomaly not having a strong enough upper PV anomaly with which to interact. Differences in the vertical structure of PV anomalies are expected at finite amplitude for two reasons. First, diabatic PV generation is weaker at finite amplitude in

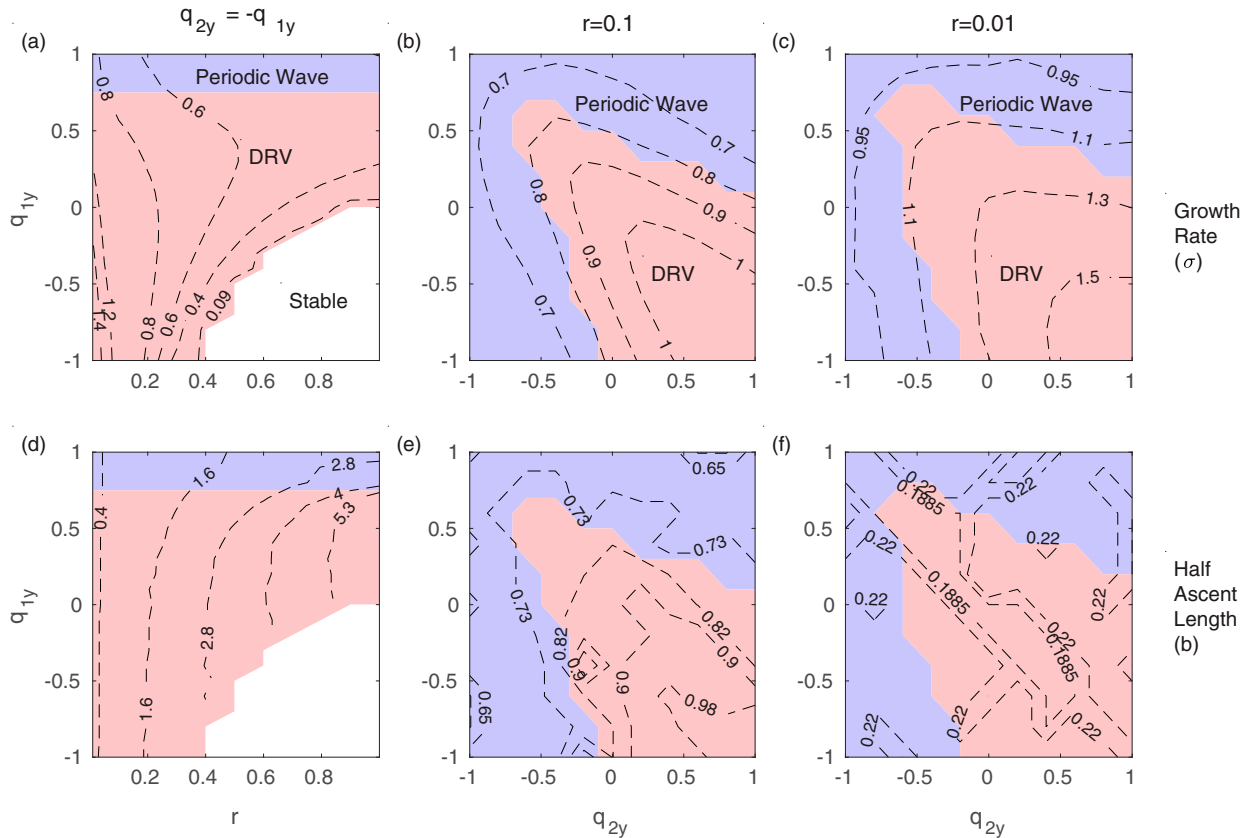


FIG. 9. Phase diagram showing whether the most unstable mode of the tilted two-layer model is a periodic wave (blue) or a DRV (red) or stable (white) for a setup where (a),(d) the PV gradients are equal and opposite in strength  $q_{1y} = -q_{2y}$  for multiple values of  $r$  and for a setup where the PV gradients vary independently from each other and (b),(e)  $r = 0.1$  or (c),(f)  $r = 0.01$ . Dashed lines in (a)–(c) show the growth rate, and dashed lines in (d)–(f) show the half-ascent length  $b$ . The domain length is  $L = 8\pi$ , and the grid spacing is  $\Delta x = 0.13$ . Note that the standard two-layer configuration has positive upper-layer PV gradient ( $q_{1y} > 0$ ) and negative lower-layer PV gradient ( $q_{2y} < 0$ ), which corresponds to the upper-left quadrants in (b), (c), (e), and (f).

anticyclonic regions, an effect that is captured in semigeostrophic models (Hoskins 1975; Emanuel et al. 1987). Second, vertical advection of PV at finite amplitude can significantly offset negative diabatic generation at upper levels because positive PV anomalies at lower levels are advected upward.

We compare the structure of the warm-climate DRV mode (Fig. 1a) with a finite-amplitude DRV storm in the same idealized GCM and climate (Fig. 1c) and with two finite-amplitude storms from reanalysis. The first storm from reanalysis is the East Coast winter storm (Fig. 10a) that was identified as a propagating and moderately growing DRV by Moore et al. (2008). It later experienced explosive growth through interaction with a preexisting upper PV anomaly, but we consider the earlier diabatic phase. The second storm from reanalysis is an example midlatitude summer cyclone (Fig. 10c) from an updated version of the DRV climatology of Boettcher and Wernli (2013) that is based on ERA5 reanalysis (Hersbach et al. 2020). It was identified as a DRV by a tracking algorithm, selecting for substantial baroclinicity, sufficient moisture, fast propagation, and weak upper-level forcing. These example storms are meant to illustrate some of the variations

in the constellation of PV anomalies and diabatic generation in observed DRVs.

Ertel PV anomalies are defined with respect to a zonal mean for the idealized GCM (using once-daily fields for the mode and 6 hourly for the macro-turbulent state) and with respect to a 4-day moving average for the 6-hourly fields from ERA5 reanalysis forecasts. The forecast mode is chosen because it provides the temperature tendencies necessary for the calculation of latent heating. The fields are first interpolated from model to pressure levels, for both GCM and reanalysis fields, prior to calculating the PV and PV generation rates.

In addition to considering the usual diabatic PV generation rate, we also consider the diabatic source of PV in isentropic coordinates according to Eq. (74a) in Hoskins et al. (1985):

$$\dot{Q}_{\text{diab}} = Q^2 \frac{\partial(\theta Q^{-1})}{\partial p} \left( \frac{\partial \theta}{\partial p} \right)^{-1}, \quad (29)$$

which we refer to as the generalized PV generation. Here  $Q$  is the potential vorticity,  $\theta$  is the potential temperature,  $\dot{\theta}$  is

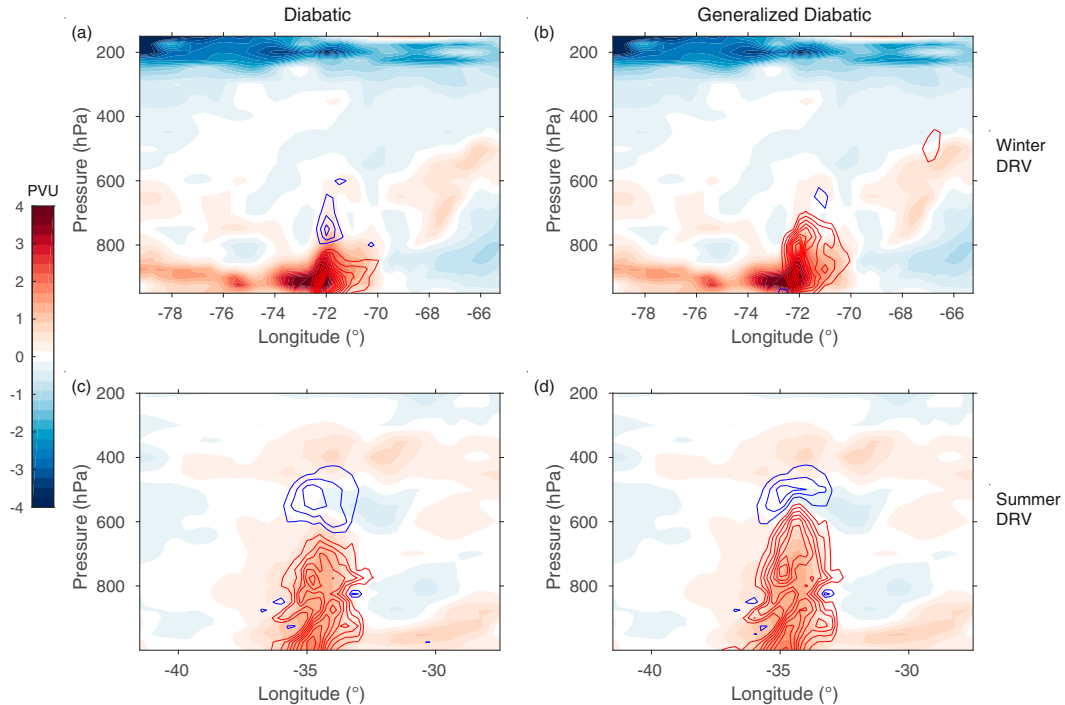


FIG. 10. The PV structure and PV generation rate due to latent heating of the (a),(b) 2005 winter storm (latitude  $37^\circ$  at 0000 UTC 25 Feb 2005) that was identified as a DRV in Moore et al. (2008), and (c),(d) an example summer cyclone (latitude  $41.25^\circ$  at 0500 UTC 10 Jul 2009) that was identified as a DRV in the climatology of Boettcher and Wernli (2013). Shading shows PV anomalies with respect to a 4-day moving average (using 6-hourly fields). Contours show (a),(c) the diabatic PV generation [the first term on the right-hand side of Eq. (30)] and (b),(d) the generalized diabatic PV generation including both diabatic PV generation and diabatic vertical advection as in Eq. (29). In all cases only diabatic effects from latent heating are included. Red contours are positive, and blue contours are negative, and the contour interval is  $0.44 \text{ pvu h}^{-1}$  for (a) and (b) and  $0.10 \text{ pvu h}^{-1}$  for (c) and (d). The zero contour line is not shown. All fields are calculated from ERA5 reanalysis, and PV is calculated using the hydrostatic approximation to Ertel's PV.

potential temperature tendency, and we have reexpressed the vertical derivatives with respect to pressure rather than potential temperature. Equation (29) may also be written as

$$\dot{Q}_{\text{diab}} = Q \frac{\partial \dot{\theta}}{\partial p} \left( \frac{\partial \theta}{\partial p} \right)^{-1} - \dot{\theta} \frac{\partial Q}{\partial p} \left( \frac{\partial \theta}{\partial p} \right)^{-1}, \quad (30)$$

which shows that the generalized PV generation combines diabatic PV generation (first term on the right-hand side) and diabatic vertical advection of PV (second term on the right-hand side).<sup>5</sup> Including vertical advection of PV is important because it can strongly offset diabatic PV generation (Büeler and Pfahl 2017; Lackmann 2002; Martínez-Alvarado et al. 2016; Stoelinga 1996; Persson 1995; Pfahl et al. 2015; Wernli and Davies 1997), and its inclusion clearly improves the match between the vertical structures of PV anomalies and PV

generation for the small-amplitude DRV mode in the idealized GCM (cf. Figs. 1a,b). In addition, considering diabatic vertical advection as part of the diabatic source of PV makes a closer connection to our QG theory in which the pseudo-PV is not advected in the vertical.

We only consider diabatic effects due to latent heating. For the idealized GCM, we have confirmed that there is no convective precipitation in the region of the finite-amplitude DRV storm, and  $\dot{\theta}$  was inferred from the large-scale condensation tendency of specific humidity, which was saved as an output field. For the reanalysis fields,  $\dot{\theta}$  was calculated from the ERA5 temperature tendency from all parameterizations in the forecast mode minus the contributions from longwave and shortwave radiation. Radiative contributions to PV generation were separately evaluated and found to be negligible.

The finite-amplitude DRVs from reanalysis (Fig. 10) do not extend as high in the atmosphere as the DRV in the warm climate of the idealized GCM, and this is as expected given that they occur in the current climate in which tropopause is lower and latent heating occurs lower in the troposphere. The generalized diabatic PV generation (contours in Figs. 10b,d) is noticeably smaller in magnitude for the upper-level negative

<sup>5</sup> An alternative approach of including vertical advection of PV in pressure coordinates (rather than diabatic vertical advection) gives similar results except that there can be additional vertical advection of PV in the upper troposphere and stratosphere in regions where latent heating is small.

generation rates as compared with lower-level positive generation rates. From the point of view of Eq. (30), the magnitude of diabatic PV generation is reduced in the upper anticyclonic region as compared with the lower cyclonic region in which  $Q$  is larger, an effect that has been seen before in the context of warm conveyor belts (Joos and Wernli 2012), and the negative diabatic PV generation is also offset by upward diabatic advection of positive PV from the positive PV anomaly lower in the atmosphere. Alternatively, from the point of view of Eq. (29), the factor of  $Q^2$  tends to be much smaller in magnitude in anticyclonic regions as compared with cyclonic regions of a finite-amplitude storm. As a result, the upper-level negative PV anomaly is weaker in magnitude than the lower-level positive PV anomaly, especially in the case of the winter storm in which it is difficult to clearly identify a negative upper-level PV anomaly that is diabatically generated.

The reason the winter storm has a greater asymmetry between lower and upper PV anomalies as compared with the summer storm seems to be because it is a stronger storm (which emphasizes the finite-amplitude effects) but also because of more subtle effects related to its vertical profile of  $\theta$  being more bottom heavy. The absence of a clear upper-level negative PV anomaly in the winter storm may reduce its growth rate at this point in its evolution, but further work would be needed to definitively link the observed growth rates and PV structures, especially given that moist baroclinic waves in the semigeostrophic Eady model have weak upper-level negative PV anomalies but can still grow strongly (Emanuel et al. 1987).

The finite-amplitude DRV in the warm-climate simulation of the idealized GCM (Figs. 1c,d) shows some similarities to the corresponding small-amplitude mode (Figs. 1a,b), although the upper-level negative PV anomaly and the generalized diabatic PV generation are considerably reduced in the storm relative to the mode for vertical levels between 300 and 500 hPa and the positive PV anomaly extends higher, both as a result of diabatic vertical advection of PV. Negative generation of PV is nonetheless strong in the upper troposphere near the tropopause, and this seems to be because of diabatic vertical advection up the mean vertical PV gradient at those levels.

Overall, our analysis of finite-amplitude DRV storms shows that finite-amplitude effects must be taken into account to relate the structure of PV anomalies and diabatic generation in observed DRVs particularly for the upper-level PV anomalies. Our results also show the value of combining diabatic PV generation and diabatic vertical advection in a generalized diabatic PV generation diagnostic (following Hoskins et al. 1985), especially when trying to connect to simpler QG models and modal solutions.

## 5. Conclusions

We have analyzed a moist two-layer QG model with conditional latent heating and tilted boundaries and shown that it is capable of producing a DRV mode. The emergence of a DRV solution in a minimal model retaining the essential physics of baroclinicity and moisture clarifies the physical

mechanisms involved and allows us to derive the first analytical expressions for the growth rate and horizontal length scale of DRVs.

A key step in our approach is the tilting of the model boundaries at a slope equal to the mean isentropes, which makes the two-layer model an analog of the interior of the Eady model in which dry-baroclinic instability has been shut off but moist instabilities are still possible. This allowed us to obtain a pure DRV solution within a conceptually simple two-layer model. PV-budget analysis revealed two distinct dynamical regimes. In the ascending branch, growth of the anomalies was maintained by diabatic heating partly offset by zonal advection, while in the descending branch growth was maintained solely by zonal advection.

We went on to derive the analytical dispersion relation for the growth rate and horizontal length scale of a DRV on an infinite domain, a significant novelty of this paper. The governing equation for the vertical velocity in the DRV is similar to the equation for the vertical velocity of moist baroclinic waves (Emanuel et al. 1987; Zurita-Gotor 2005) except for the presence of two extra terms that lead to isolated rather than periodic solutions—a distinctive characteristic of the DRV. Analytic solutions to the dispersion equations were found in the limit of small static-stability reduction factor (i.e., in the limit in which the stratification is neutral to moist convection). While the ascent length remains the same for the DRV as for the moist wave solutions of Emanuel et al. (1987) in this limit, the DRV grows faster by 54% as compared with the moist wave. This faster growth is consistent with the fact that the DRV emerged as the fastest-growing solution in the moist baroclinic instability simulations of O'Gorman et al. (2018) in a warm climate with small moist static stability. Root solving of the dispersion equations for a larger range of  $r$  values showed that physical solutions cease to exist when  $r > 0.38$ . This is an indication that isolated DRV disturbances cannot exist on an infinite domain when the moist static stability is not small enough.

Including nonzero meridional PV gradients in the tilted two-layer model and varying their strengths and varying the moist static stability (as represented by the reduction factor  $r$ ), we showed that isolated DRV solutions emerge even in more realistic model setups and are not an artifact of the assumption of zero PV gradients in our simplest version of the tilted two-layer model. The most unstable mode transitions from periodic waves to isolated DRVs when the magnitude of the PV gradients is weakened or entirely reversed relative to the standard two-layer setup. This suggests that the vertical structure of meridional PV gradients may be an important additional factor that helps to determine DRV genesis zones in addition to small moist static stability. Weak QG PV gradients can be found particularly at polar latitudes in the current climate, which could help strengthen the links that have been previously established between the growth mechanism of DRVs and polar lows (Montgomery and Farrell 1991, 1992; Moore and Montgomery 2005; Moreno-Ibáñez et al. 2021).

The stark transition from periodic wave solutions to isolated DRV disturbances when diabatic heating becomes more important than meridional PV advection was also explained

qualitatively using “PV thinking”: in a diabatically dominated regime, the asymmetry of the diabatic heating regenerates only positive PV anomalies in the lower layer and negative PV anomalies in the upper layer. However, a series of like-signed PV anomalies in each layer leads to weaker meridional flow between the PV anomalies than occurs for a single PV dipole consisting of one anomaly in each layer. Thus the single PV dipole has stronger ascent and latent heating and emerges as the fastest-growing mode of the system.

Last, we compared the structure of small-amplitude DRV modes with finite-amplitude storms from reanalysis in winter and summer and from a warm-climate simulation in an idealized GCM. The finite-amplitude storms have similarities with the small-amplitude DRV modes but also some differences. In the storms from reanalysis, the upper-level negative PV anomaly is substantially weaker than the lower-level positive PV anomaly. This asymmetry arises because diabatic PV generation is weaker in anticyclonic regions at finite amplitude, and also because upward PV advection from the positive PV anomaly at lower levels can offset the upper-level negative PV generation. For the finite-amplitude DRV in the warm climate of the idealized GCM, vertical advection of the mean vertical PV gradient near the tropopause meant there was still a strong upper-level negative PV anomaly. In the case of the winter storm, the upper-level PV anomaly was sufficiently weak that it was difficult to identify, and we hypothesize that a weak upper-level PV anomaly may explain why some DRV storms in the current climate propagate but do not grow strongly. This hypothesis could be tested in future work with a semigeostrophic model that has sufficient vertical levels to accurately resolve vertical PV advection, and by tracking DRVs across a range of climates in idealized GCM simulations to study the relationship between growth rates and the structure of the PV anomalies.

Future work could also investigate whether a DRV solution and wave-vortex transition can also be isolated within a continuous Eady model in which dry baroclinic instability is eliminated by removing the upper lid. This setup is likely no longer tractable analytically (because solutions are no longer separable in the presence of nonlinear heating; Zurita-Gotor 2005), but a numerical analysis would make for a useful extension of this work, in which realistic features such as near surface temperature advection, vertically dependent drag and vertically dependent static stability reduction factor could be more readily incorporated.

*Acknowledgments.* We acknowledge helpful discussions with Santiago Benavides, Andre da Silva, Minmin Fu, Martín Vélez-Pardo, Stephan Pfahl, Kerry Emanuel, Glenn Flierl, Maxi Boettcher, Heini Wernli, and Raymond Pierrehumbert. We thank Maxi Boettcher and Heini Wernli for providing us with the database of tracked DRVs from reanalysis. We are grateful to an anonymous reviewer, Heini Wernli, and Michael T. Montgomery for their helpful comments. We acknowledge support from NSF AGS 2031472 and the mTerra Catalyst Fund.

*Data availability statement.* ERA5 data are available from ECMWF (<https://cds.climate.copernicus.eu>), and code for the tilted two-layer model calculations is available on GitHub ([https://github.com/matthieukohl/DRV\\_Paper](https://github.com/matthieukohl/DRV_Paper)).

## APPENDIX A

### Derivation of the Tilted Two-Layer Model

We discretize the moist-quasigeostrophic equations on an  $f$  plane [Eqs. (1) and (2)] in the vertical taking into account the tilted boundaries  $h_1(y)$  and  $h_2(y)$  through a modified boundary condition on  $w$  at the top and bottom (Fig. A1). For the vorticity equations in the two layers we obtain

$$\partial_t \nabla^2 \psi_1 + J(\psi_1, \nabla^2 \psi_1) - \frac{f}{H} [J(\psi_1, h_1) - w] = 0 \quad \text{and} \quad (\text{A1})$$

$$\partial_t \nabla^2 \psi_2 + J(\psi_2, \nabla^2 \psi_2) - \frac{f}{H} [w - J(\psi_2, h_2)] = 0. \quad (\text{A2})$$

Adding and subtracting give vorticity equations in terms of the barotropic streamfunction  $\phi$  and baroclinic streamfunction  $\tau$ :

$$\begin{aligned} \partial_t \nabla^2 \phi + J(\phi, \nabla^2 \phi) + J(\tau, \nabla^2 \tau) - \frac{f}{2H} J(\phi, h_1 - h_2) \\ - \frac{f}{2H} J(\tau, h_1 + h_2) = 0, \quad \text{and} \end{aligned} \quad (\text{A3})$$

$$\begin{aligned} \partial_t \nabla^2 \tau + J(\phi, \nabla^2 \tau) + J(\tau, \nabla^2 \phi) + \frac{f}{H} w - \frac{f}{2H} J(\phi, h_1 + h_2) \\ - \frac{f}{2H} J(\tau, h_1 - h_2) = 0. \end{aligned} \quad (\text{A4})$$

Discretizing the thermodynamic equation in the vertical, we obtain

$$\partial_t \tau + J(\phi, \tau) + \frac{N^2 H}{2f} r(w)w = \frac{N^2 H}{2f} \overline{r(w)w}. \quad (\text{A5})$$

We nondimensionalize using  $x, y \sim L_D$ , where  $L_D = NH/(\sqrt{2}f)$  is the deformation radius with individual layer height  $H$ ,  $z \sim H$ ,  $u$  and  $v \sim U$ ,  $w \sim U^2 H / (f L_D^2)$ ,  $\phi = \tau \sim U L_D$ ,  $t \sim L_D U$ , and  $h_1$  and  $h_2 \sim UH / (f L_D)$  to obtain

$$\begin{aligned} \partial_t \nabla^2 \phi + J(\phi, \nabla^2 \phi) + J(\tau, \nabla^2 \tau) - \frac{1}{2} J(\phi, h_1 - h_2) \\ - \frac{1}{2} J(\tau, h_1 + h_2) = 0, \end{aligned} \quad (\text{A6})$$

$$\begin{aligned} \partial_t \nabla^2 \tau + J(\phi, \nabla^2 \tau) + J(\tau, \nabla^2 \phi) + w - \frac{1}{2} J(\phi, h_1 + h_2) \\ - \frac{1}{2} J(\tau, h_1 - h_2) = 0, \quad \text{and} \end{aligned} \quad (\text{A7})$$

$$\partial_t \tau + J(\phi, \tau) + r(w)w = \overline{r(w)w}, \quad (\text{A8})$$

where all variables are now nondimensional. We next assume small-amplitude perturbations about the basic state  $\tau_0 = -y$  and  $\phi_0 = 0$  corresponding to a shear flow  $u_1 = 1$

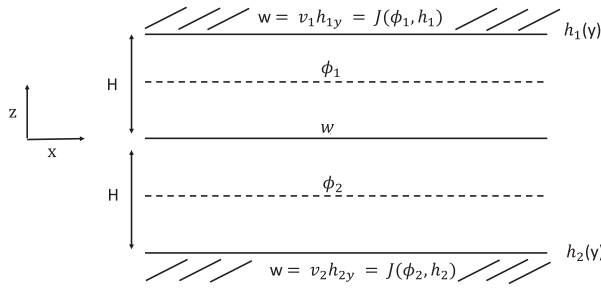


FIG. A1. Schematic of the tilted two-layer model in the  $x$ - $z$  plane.

and  $u_2 = -1$  such that the advection terms are linearized. Note, however, that the thermodynamic equation remains nonlinear because of the nonlinear dependence of  $r(w)$  on  $w$ . Using the tilted boundary conditions  $h_1 = h_2 = y$  and assuming that the perturbations are independent of  $y$  gives the perturbation Eqs. (4)–(6). If instead we assume  $h_1 = \alpha_1 y$  and  $h_2 = \alpha_2 y$ , we obtain the perturbation Eqs. (26)–(28).

APPENDIX B

Derivation of the Equation for  $w$

Starting from Eqs. (9)–(11), we first take two derivatives of Eq. (11) and subtract Eq. (10) to get

$$[r(w)w]_{xx} - w = 2\phi_{xxx} - \phi_x. \tag{B1}$$

Multiplying Eq. (9) by  $\sigma$  and taking one derivative, and substituting for  $\tau_{xx}$  and  $\tau_{xxx}$  using Eq. (10), we find

$$w - w_{xx} + \sigma^2\phi_{xxx} - \phi_{xxxx} + 2\phi_{xxx} - \phi_x = 0, \tag{B2}$$

where the last two terms  $2\phi_{xxx} - \phi_x$  can be substituted using Eq. (B1) to give

$$[r(w)w]_{xx} - w_{xx} = \phi_{xxxx} - \sigma^2\phi_{xxx}. \tag{B3}$$

Double integration of Eq. (B3) yields the relation

$$r(w)w - w = \phi_{xxx} - \sigma^2\phi_x + \overline{r(w)w}, \tag{B4}$$

where we have used mass conservation ( $\bar{w} = 0$ ) to choose the integration constant (this relation will be necessary as a substitution at the end of the derivation). Taking two derivatives of Eq. (B1) and subtracting Eq. (B3) twice gives

$$[r(w)w]_{xxxx} - 2[r(w)w]_{xx} + w_{xx} = 2\sigma^2\phi_{xxx} - \phi_{xxx}. \tag{B5}$$

Subtracting Eq. (B1) multiplied by  $\sigma^2$  from Eq. (B5), we get

$$[r(w)w]_{xxxx} - (2 + \sigma^2)[r(w)w]_{xx} + w_{xx} + \sigma^2w = -\phi_{xxx} + \sigma^2\phi_x. \tag{B6}$$

Using Eq. (B4) allows us to substitute the last  $\phi$  terms in Eq. (B6) to finally obtain Eq. (12), which is an equation in  $w$  only.

APPENDIX C

Mass Conservation for a DRV on an Infinite Domain

Imposing mass conservation  $\int_0^L w dx = 0$  on the solution defined by Eqs. (13) and (14) and using Eq. (17) yields

$$\begin{aligned} & \frac{ab}{r + \sigma^2 - 1} + \frac{c_1}{k_1} \sin(k_1 b) + \frac{c_2}{k_2} \sin(k_2 b) \\ & + \frac{a}{\sigma^2}(L - b) + \frac{a}{\sigma^2}[e^{-\sigma(L-b)} - 1] \\ & + d_2 \left\{ -\frac{1}{\sigma}[e^{-\sigma(L-b)} - 1] + [e^{-(L-b)} - 1] \right\} = 0. \tag{C1} \end{aligned}$$

We are interested in the infinite-domain limit  $L \rightarrow \infty$ . It is important that we took the integral in  $x$  to obtain Eq. (C1) prior to taking the limit  $L \rightarrow \infty$  (i.e., taking the limit of the statement of mass conservation) because the order of taking the limit and integral affects the result. As shown in section 2c, the definition of  $a$  together with mass conservation implies that

$$a = \frac{1}{L} \int_0^b (r - 1)w_1 dx$$

such that  $a \rightarrow 0$  if we want solutions for which  $b$  and  $w_1$  remain bounded. This leaves us with the indeterminate term  $aL$  in the mass conservation equation [Eq. (C1)]. We can eliminate this term by using

$$\begin{aligned} aL &= \int_0^b (r - 1)w_1 dx \\ &= (r - 1) \left[ \frac{ab}{r + \sigma^2 - 1} + \frac{c_1}{k_1} \sin(k_1 b) + \frac{c_2}{k_2} \sin(k_2 b) \right] \tag{C2} \end{aligned}$$

to arrive at a form of the mass conservation condition that does not involve  $aL$ :

$$\begin{aligned} & \frac{ab}{\sigma^2 + r - 1} + \frac{c_1}{k_1} \sin(k_1 b) + \frac{c_2}{k_2} \sin(k_2 b) \\ & + \frac{r - 1}{\sigma^2} \left[ \frac{ab}{\sigma^2 + r - 1} + \frac{c_1}{k_1} \sin(k_1 b) + \frac{c_2}{k_2} \sin(k_2 b) \right] \\ & - \frac{ab}{\sigma^2} + \frac{a}{\sigma^2}[e^{-(L-b)} - 1] \\ & + d_2 \left\{ -\frac{1}{\sigma}[e^{-\sigma(L-b)} - 1] + [e^{-(L-b)} - 1] \right\} = 0. \tag{C3} \end{aligned}$$

We can now take the limit  $L \rightarrow \infty$  and  $a \rightarrow 0$  to arrive at Eq. (21) in the main text. For completeness we note that by substituting Eq. (21) into Eq. (C2), and taking the limit  $L \rightarrow \infty$  and  $a \rightarrow 0$ , we obtain the expression

$$aL = d_2 \frac{(r-1)\sigma(\sigma-1)}{r+\sigma^2-1}. \tag{C4}$$

$$\tan\left(b\sqrt{\sigma_0^2-1}\right) = \frac{\sqrt{\sigma_0^2-1}(1-\sigma_0^2+\sigma_0)}{(1+\sigma_0)(\sigma_0^2-1)}. \tag{E2}$$

APPENDIX D

Derivation of the Dispersion Relation

To derive the dispersion relation from the constraints [Eqs. (18)–(21)], we write the constraints solely in terms of equations for  $c_1$  and  $c_2$ . Writing Eqs. (18) and (20) as

$$\begin{pmatrix} 1 & 1 \\ k_1^2 & k_2^2 \end{pmatrix} \begin{bmatrix} c_1 \cos(k_1 b) \\ c_2 \cos(k_2 b) \end{bmatrix} = d_2 \begin{pmatrix} 0 \\ \frac{1-\sigma^2}{r} \end{pmatrix}, \tag{D1}$$

and inverting, we obtain

$$\begin{bmatrix} c_1 \cos(k_1 b) \\ c_2 \cos(k_2 b) \end{bmatrix} = \frac{d_2}{k_2^2 - k_1^2} \begin{pmatrix} k_2^2 & -1 \\ -k_1^2 & 1 \end{pmatrix} \begin{pmatrix} 0 \\ \frac{1-\sigma^2}{r} \end{pmatrix}. \tag{D2}$$

Similarly, writing Eqs. (19) and (21) as

$$\begin{pmatrix} k_1 & k_2 \\ 1/k_1 & 1/k_2 \end{pmatrix} \begin{bmatrix} c_1 \sin(k_1 b) \\ c_2 \sin(k_2 b) \end{bmatrix} = d_2 \begin{pmatrix} \frac{\sigma-1}{r} \\ \frac{\sigma(\sigma-1)}{\sigma^2+r-1} \end{pmatrix}, \tag{D3}$$

and inverting, we obtain

$$\begin{bmatrix} c_1 \sin(k_1 b) \\ c_2 \sin(k_2 b) \end{bmatrix} = \frac{d_2 k_1 k_2}{k_1^2 - k_2^2} \begin{pmatrix} 1/k_2 & -k_2 \\ -1/k_1 & k_1 \end{pmatrix} \begin{pmatrix} \frac{\sigma-1}{r} \\ \frac{\sigma(\sigma-1)}{\sigma^2+r-1} \end{pmatrix}. \tag{D4}$$

Dividing the equations for  $c_i \sin k_i b$  and  $c_i \cos k_i b$ , with  $i = 1, 2$ , by each other, we obtain the two “tan” equations that form the dispersion relation [Eqs. (22) and (23)] in section 2c.

APPENDIX E

Asymptotic Expressions for Growth Rate and Half-Ascent Length

In the limit  $r \ll 1$ , the wavenumbers can be simplified to  $k_1 = 1/\sqrt{r} + O(\sqrt{r})$  and  $k_2 = \sqrt{\sigma^2-1} + O(r)$ , where we assume that  $\sigma = \sigma_0$  is an  $O(1)$  quantity to be determined. Plugging these expressions into the two tangent Eqs. (22) and (23) that form the dispersion relation we obtain to leading order:

$$\tan\left(\frac{b}{\sqrt{r}}\right) = -\frac{1}{\sqrt{r}(1+\sigma_0)} \quad \text{and} \tag{E1}$$

The right-hand side of Eq. (E1) tends to  $-\infty$  as  $r$  becomes small. To balance it, we use the *ansatz*  $b/\sqrt{r} = \pi/2 + \epsilon$ , where  $\epsilon \rightarrow 0$  as  $r \rightarrow 0$ , from which we obtain

$$\tan\left(\frac{\pi}{2} + \epsilon\right) \approx -1/\epsilon = -\frac{1}{\sqrt{r}(1+\sigma_0)}, \tag{E3}$$

which gives  $\epsilon = \sqrt{r}(1+\sigma_0)$  and  $b = (\pi/2)\sqrt{r} + r(1+\sigma_0)$  such that to leading order

$$b = \frac{\pi}{2}\sqrt{r}. \tag{E4}$$

Linearizing the tangent in Eq. (E2) we obtain

$$b = \frac{1-\sigma_0(\sigma_0-1)}{(1+\sigma_0)(\sigma_0^2-1)}. \tag{E5}$$

Since  $b$  is  $O(\sqrt{r})$  but the right-hand side of Eq. (E5) is  $O(1)$ , the right-hand side must vanish. Thus  $1-\sigma_0(\sigma_0-1) = 0$ , which implies for growing solutions  $\sigma_0 > 0$  that

$$\sigma_0 = \frac{1+\sqrt{5}}{2} = 1.62. \tag{E6}$$

REFERENCES

Bembenek, E., D. N. Straub, and T. M. Merlis, 2020: Effects of moisture in a two-layer model of the midlatitude jet stream. *J. Atmos. Sci.*, **77**, 131–147, <https://doi.org/10.1175/JAS-D-19-0021.1>.

Boettcher, M., and H. Wernli, 2013: A 10-yr climatology of diabatic Rossby waves in the Northern Hemisphere. *Mon. Wea. Rev.*, **141**, 1139–1154, <https://doi.org/10.1175/MWR-D-12-00012.1>.

Booth, J. F., L. Polvani, P. A. O’Gorman, and S. Wang, 2015: Effective stability in a moist baroclinic wave. *Atmos. Sci. Lett.*, **16**, 56–62, <https://doi.org/10.1002/asl2.520>.

Bretherton, F. P., 1966: Baroclinic instability and the short wavelength cut-off in terms of potential vorticity. *Quart. J. Roy. Meteor. Soc.*, **92**, 335–345, <https://doi.org/10.1002/qj.49709239303>.

Büeler, D., and S. Pfahl, 2017: Potential vorticity diagnostics to quantify effects of latent heating in extratropical cyclones. Part I: Methodology. *J. Atmos. Sci.*, **74**, 3567–3590, <https://doi.org/10.1175/JAS-D-17-0041.1>.

Charney, J. G., 1947: The dynamics of long waves in a baroclinic westerly current. *J. Atmos. Sci.*, **4**, 136–162, [https://doi.org/10.1175/1520-0469\(1947\)004<0136:tdolwi>2.0.co;2](https://doi.org/10.1175/1520-0469(1947)004<0136:tdolwi>2.0.co;2).

Eady, E. T., 1949: Long waves and cyclone waves. *Tellus*, **1** (3), 33–52, <https://doi.org/10.3402/tellusa.v1i3.8507>.

Emanuel, K. A., M. Fantini, and A. J. Thorpe, 1987: Baroclinic instability in an environment of small stability to slantwise moist convection. Part I: Two-dimensional models. *J. Atmos. Sci.*,

- 44, 1559–1573, [https://doi.org/10.1175/1520-0469\(1987\)044<1559:BIIAEO>2.0.CO;2](https://doi.org/10.1175/1520-0469(1987)044<1559:BIIAEO>2.0.CO;2).
- Fantini, M., 1995: Moist Eady waves in a quasigeostrophic three-dimensional model. *J. Atmos. Sci.*, **52**, 2473–2485, [https://doi.org/10.1175/1520-0469\(1995\)052<2473:MEWIAQ>2.0.CO;2](https://doi.org/10.1175/1520-0469(1995)052<2473:MEWIAQ>2.0.CO;2).
- Fjørtoft, R., 1950: *Application of Integral Theorems in Deriving Criteria of Stability for Laminar Flows and for the Baroclinic Circular Vortex*. Vol. 17, Grøndahl and Sønns Boktr, 52 pp.
- Hersbach, H., and Coauthors, 2020: The ERA5 global reanalysis. *Quart. J. Roy. Meteor. Soc.*, **146**, 1999–2049, <https://doi.org/10.1002/qj.3803>.
- Hoskins, B. J., 1975: Geostrophic momentum approximation and the semi-geostrophic equations. *J. Atmos. Sci.*, **32**, 233–242, [https://doi.org/10.1175/1520-0469\(1975\)032<0233:TGMAAT>2.0.CO;2](https://doi.org/10.1175/1520-0469(1975)032<0233:TGMAAT>2.0.CO;2).
- , M. E. McIntyre, and A. W. Robertson, 1985: On the use and significance of isentropic potential vorticity maps. *Quart. J. Roy. Meteor. Soc.*, **111**, 877–946, <https://doi.org/10.1002/qj.49711147002>.
- Joos, H., and H. Wernli, 2012: Influence of microphysical processes on the potential vorticity development in a warm conveyor belt: A case-study with the limited-area model COSMO. *Quart. J. Roy. Meteor. Soc.*, **138**, 407–418, <https://doi.org/10.1002/qj.934>.
- Lackmann, G. M., 2002: Cold-frontal potential vorticity maxima, the low-level jet, and moisture transport in extratropical cyclones. *Mon. Wea. Rev.*, **130**, 59–74, [https://doi.org/10.1175/1520-0493\(2002\)130<0059:CFPVMT>2.0.CO;2](https://doi.org/10.1175/1520-0493(2002)130<0059:CFPVMT>2.0.CO;2).
- Lambaerts, J., G. Lapeyre, and V. Zeitlin, 2012: Moist versus dry baroclinic instability in a simplified two-layer atmospheric model with condensation and latent heat release. *J. Atmos. Sci.*, **69**, 1405–1426, <https://doi.org/10.1175/JAS-D-11-0205.1>.
- Lapeyre, G., and I. M. Held, 2004: The role of moisture in the dynamics and energetics of turbulent baroclinic eddies. *J. Atmos. Sci.*, **61**, 1693–1710, [https://doi.org/10.1175/1520-0469\(2004\)061<1693:tromit>2.0.co;2](https://doi.org/10.1175/1520-0469(2004)061<1693:tromit>2.0.co;2).
- Martínez-Alvarado, O., S. L. Gray, and J. Methven, 2016: Diabatic processes and the evolution of two contrasting summer extratropical cyclones. *Mon. Wea. Rev.*, **144**, 3251–3276, <https://doi.org/10.1175/MWR-D-15-0395.1>.
- Montgomery, M. T., and B. F. Farrell, 1991: Moist surface frontogenesis associated with interior potential vorticity anomalies in a semigeostrophic model. *J. Atmos. Sci.*, **48**, 343–368, [https://doi.org/10.1175/1520-0469\(1991\)048<0343:msfawi>2.0.co;2](https://doi.org/10.1175/1520-0469(1991)048<0343:msfawi>2.0.co;2).
- , and —, 1992: Polar low dynamics. *J. Atmos. Sci.*, **49**, 2484–2505, [https://doi.org/10.1175/1520-0469\(1992\)049<2484:PLD>2.0.CO;2](https://doi.org/10.1175/1520-0469(1992)049<2484:PLD>2.0.CO;2).
- Moore, R. W., and M. T. Montgomery, 2004: Reexamining the dynamics of short-scale, diabatic Rossby waves and their role in midlatitude moist cyclogenesis. *J. Atmos. Sci.*, **61**, 754–768, [https://doi.org/10.1175/1520-0469\(2004\)061<0754:RTDOSD>2.0.CO;2](https://doi.org/10.1175/1520-0469(2004)061<0754:RTDOSD>2.0.CO;2).
- , and —, 2005: Analysis of an idealized, three-dimensional diabatic Rossby vortex: A coherent structure of the moist baroclinic atmosphere. *J. Atmos. Sci.*, **62**, 2703–2725, <https://doi.org/10.1175/JAS3472.1>.
- , —, and H. C. Davies, 2008: The integral role of a diabatic Rossby vortex in a heavy snowfall event. *Mon. Wea. Rev.*, **136**, 1878–1897, <https://doi.org/10.1175/2007MWR2257.1>.
- Moreno-Ibáñez, M., R. Laprise, and P. Gachon, 2021: Recent advances in polar low research: Current knowledge, challenges and future perspectives. *Tellus*, **73A**, 1890412, <https://doi.org/10.1080/16000870.2021.1890412>.
- O'Gorman, P. A., 2011: The effective static stability experienced by eddies in a moist atmosphere. *J. Atmos. Sci.*, **68**, 75–90, <https://doi.org/10.1175/2010JAS3537.1>.
- , T. M. Merlis, and M. S. Singh, 2018: Increase in the skewness of extratropical vertical velocities with climate warming: Fully nonlinear simulations versus moist baroclinic instability. *Quart. J. Roy. Meteor. Soc.*, **144**, 208–217, <https://doi.org/10.1002/qj.3195>.
- Parker, D. J., and A. J. Thorpe, 1995: Conditional convective heating in a baroclinic atmosphere: A model of convective frontogenesis. *J. Atmos. Sci.*, **52**, 1699–1711, [https://doi.org/10.1175/1520-0469\(1995\)052<1699:CCHIAB>2.0.CO;2](https://doi.org/10.1175/1520-0469(1995)052<1699:CCHIAB>2.0.CO;2).
- Pedlosky, J., 1964: The stability of currents in the atmosphere and the ocean: Part I. *J. Atmos. Sci.*, **21**, 201–219, [https://doi.org/10.1175/1520-0469\(1964\)021<0201:TSOCIT>2.0.CO;2](https://doi.org/10.1175/1520-0469(1964)021<0201:TSOCIT>2.0.CO;2).
- Persson, P. O. G., 1995: Simulations of the potential vorticity structure and budget of fronts 87 IOP8. *Quart. J. Roy. Meteor. Soc.*, **121**, 1041–1081, <https://doi.org/10.1002/qj.49712152506>.
- Pfahl, S., P. A. O'Gorman, and M. S. Singh, 2015: Extratropical cyclones in idealized simulations of changed climates. *J. Climate*, **28**, 9373–9392, <https://doi.org/10.1175/JCLI-D-14-00816.1>.
- Phillips, N. A., 1954: Energy transformations and meridional circulations associated with simple baroclinic waves in a two-level, quasi-geostrophic model. *Tellus*, **6**, 273–286, <https://doi.org/10.1111/j.2153-3490.1954.tb01123.x>.
- Snyder, C., and R. S. Lindzen, 1991: Quasi-geostrophic wave-CISK in an unbounded baroclinic shear. *J. Atmos. Sci.*, **48**, 76–86, [https://doi.org/10.1175/1520-0469\(1991\)048<0076:QGWICIA>2.0.CO;2](https://doi.org/10.1175/1520-0469(1991)048<0076:QGWICIA>2.0.CO;2).
- Stoelinga, M. T., 1996: A potential vorticity-based study of the role of diabatic heating and friction in a numerically simulated baroclinic cyclone. *Mon. Wea. Rev.*, **124**, 849–874, [https://doi.org/10.1175/1520-0493\(1996\)124<0849:APVBSO>2.0.CO;2](https://doi.org/10.1175/1520-0493(1996)124<0849:APVBSO>2.0.CO;2).
- Tierney, G., D. J. Posselt, and J. F. Booth, 2018: An examination of extratropical cyclone response to changes in baroclinicity and temperature in an idealized environment. *Climate Dyn.*, **51**, 3829–3846, <https://doi.org/10.1007/s00382-018-4115-5>.
- Wernli, H., and H. C. Davies, 1997: A Lagrangian-based analysis of extratropical cyclones. I: The method and some applications. *Quart. J. Roy. Meteor. Soc.*, **123**, 467–489, <https://doi.org/10.1002/qj.49712353811>.
- , S. Dirren, M. A. Liniger, and M. Zillig, 2002: Dynamical aspects of the life cycle of the winter storm 'Lothar' (26–26 December 1999). *Quart. J. Roy. Meteor. Soc.*, **128**, 405–429, <https://doi.org/10.1256/003590002321042036>.
- Whitaker, J. S., and C. A. Davis, 1994: Cyclogenesis in a saturated environment. *J. Atmos. Sci.*, **51**, 889–908, [https://doi.org/10.1175/1520-0469\(1994\)051<0889:ciase>2.0.co;2](https://doi.org/10.1175/1520-0469(1994)051<0889:ciase>2.0.co;2).
- Zurita-Gotor, P., 2005: Updraft/downdraft constraints for moist baroclinic modes and their implications for the short-wave cutoff and maximum growth rate. *J. Atmos. Sci.*, **62**, 4450–4458, <https://doi.org/10.1175/JAS3630.1>.